AZIMUTHAL MODULATIONAL INSTABILITY OF VORTEX SOLUTIONS TO THE TWO DIMENSIONAL NONLINEAR SCHRÖDINGER EQUATION

A Thesis

Presented to the

Faculty of

San Diego State University

In Partial Fulfillment

of the Requirements for the Degree

Master of Science

in

Computational Science

---

by

Ronald Meyer Caplan

May 2008

SAN DIEGO STATE UNIVERSITY

The Undersigned Faculty Committee Approves the

Thesis of Ronald Meyer Caplan:

Azimuthal Modulational Instability

of Vortex Solutions to the

Two Dimensional Nonlinear Schrödinger Equation

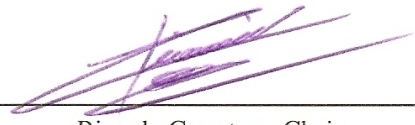

Ricardo Carretero, Chair
Department of Mathematics and Statistics

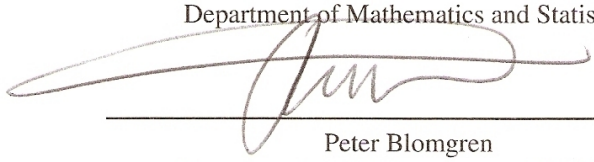

Peter Blomgren
Department of Mathematics and Statistics

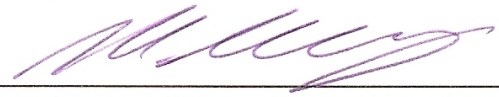

Michael Bromley
Department of Physics

04-Apr-2008

Approval Date

Copyright 2008
by
Ronald Meyer Caplan

How abundant are your works Lord, all of them You made with wisdom, the Earth is full of Your possessions.

- Psalms 104:24

See, this I have discovered, said Koheles, adding one to one to find a calculation.

- Ecclesiastes 7:27

ABSTRACT OF THE THESIS

Azimuthal Modulational Instability
of Vortex Solutions to the
Two Dimensional Nonlinear Schrödinger Equation
by
Ronald Meyer Caplan
Master of Science in Computational Science
San Diego State University, 2008

We study the azimuthal modulational instability (MI) of vortices with different topological charges, in the focusing two-dimensional nonlinear Schrödinger (NLS) equation. This setting has direct application in the realm of Bose-Einstein condensates and light propagation in nonlinear crystals.

The method of studying the stability relies on freezing the radial direction in the Lagrangian functional of the NLS in order to form a quasi-one-dimensional azimuthal equation of motion, and then applying a stability analysis in Fourier space of the azimuthal modes. We formulate predictions of growth rates of individual modes and find that vortices are unstable below a critical azimuthal wave number.

Steady state vortex solutions are found by first using a variational approach to obtain an asymptotic analytical ansatz, and then using it as an initial condition to a nonlinear equation numerical optimization routine. The stability analysis predictions are corroborated by direct numerical simulations of the NLS performed on a polar coordinate finite-difference scheme.

We briefly show how to extend the method to encompass nonlocal nonlinearities that tend to stabilize solutions.

TABLE OF CONTENTS

PAGE

ABSTRACT v

LIST OF TABLES viii

LIST OF FIGURES ix

ACKNOWLEDGEMENTS xi

CHAPTER

1 INTRODUCTION 1

1.1 Background and Motivation 1

1.2 Purpose 5

1.3 Procedure 6

2 THE MODEL 7

2.1 Two-Dimensional Nonlinear Schrödinger Equation 7

2.2 Azimuthal Equation of Motion 9

3 STABILITY ANALYSIS 12

3.1 Simplifications and Dispersion Relation 12

3.2 Perturbation Method 13

3.3 Linear Stability Analysis 14

4 FINDING STEADY-STATE VORTEX SOLUTIONS 17

4.1 Variational Approach 17

4.2 Numerical Optimization 18

4.3 Asymptotic Analytic Solution for High Charges 23

4.4 Solution Invariance 25

5 THEORETICAL PREDICTIONS 28

5.1 Analytical Predictions 28

5.2 Numerical Predictions 30

5.3 Analytical and Numerical Comparisons 33

6 NUMERICAL METHOD 36

6.1 Finite Difference on a Polar Grid 36

6.2 Boundary Conditions 38

6.3 Initial Conditions 39
6.4 Growth Rate Computation 41
7 NUMERICAL RESULTS 45
7.1 Integration of the Azimuthal Equation 45
7.2 Integration of Full Two-Dimensional System 47
8 THEORETICAL EXTENSION: THE NONLOCAL CASE 58
8.1 Nonlocal Model 58
8.2 Stability Analysis 59
9 CONCLUSION 60
9.1 Summary of Results 60
9.2 Further Extensions 60
BIBLIOGRAPHY 62

LIST OF TABLES

PAGE

Table 5.1 Numerical and Analytical Predictions of Growth Rates for $K = 1, ..., 9$ and $m = 1, ..., 5$ with Percent Difference. 35

Table 7.1 Numerical Results and Predictions for $m = 1$ and $K = 1, ..., 9$ with Percent Error. 52

Table 7.2 Numerical Results and Predictions for $m = 2$ and $K = 1, ..., 9$ with Percent Error. 53

Table 7.3 Numerical Results and Predictions for $m = 3$ and $K = 1, ..., 9$ with Percent Error. 55

Table 7.4 Numerical Results and Predictions for $m = 4$ and $K = 1, ..., 9$ with Percent Error. 56

Table 7.5 Numerical Results and Predictions for $m = 5$ and $K = 1, ..., 9$ with Percent Error. 57

LIST OF FIGURES

PAGE

Figure 1.1 An example of a two-dimensional vortex solution to the focusing NLS. 3
Figure 1.2 An experimental example of a BEC vortex 4
Figure 1.3 Examples of experimental optical vortices of different charges. 4
Figure 1.4 Simulated example of blow up due to MI of a vortex. 5
Figure 2.1 Eigenmodes of several vortices. 9
Figure 3.1 Phase portrait of Eq. (3.11) for $K_{\text{crit}} = 5$. 15
Figure 4.1 Discretization of radial direction 19
Figure 4.2 Example of numerical optimization process. 20
Figure 4.3 Initial condition and numerical solution of radial profile. 22
Figure 4.4 Sample vortices showing an increased radius for an increased charge. 23
Figure 4.5 Comparison between VA2 and GN solutions 26
Figure 5.1 Analytical predictions of growth rates for $m = 1, ..., 5$ using VA2 30
Figure 5.2 Relative error in numerically integrating Ω for $m = 1, ..., 60$ 31
Figure 5.3 Numerical predictions of growth rates for $m = 1, ..., 5$ using GN optimization. 32
Figure 5.4 Error between numerical and analytical predictions of K_{crit} and λ_{max}. 34
Figure 6.1 Example of a discretized polar coordinate grid. 36
Figure 6.2 Illustration of central radius crest extraction. 41
Figure 6.3 Example plot of growth of perturbed mode. 42
Figure 6.4 Example plot of growth rate of perturbed mode. 43
Figure 7.1 Growth rates for off-eigenvector initial condition. 46
Figure 7.2 Growth rates for eigenvector initial condition. 48
Figure 7.3 Growth rate using eigenvector initial condition and a resolution of 500. 49
Figure 7.4 Examples of perturbed vortices. 50
Figure 7.5 Evolution for the values of the critical mode and prefactor of the growth rates over an unperturbed simulation of an $m = 1$ vortex. 51
Figure 7.6 Growth rates from simulation and predictions for $m = 1$. 52
Figure 7.7 Growth rates from simulation and predictions for $m = 2$. 53
Figure 7.8 Growth rates from simulation and predictions for $m = 3$. 55

Figure 7.9 Growth rates from simulation and predictions for $m = 4$. 56
Figure 7.10 Growth rates from simulation and predictions for $m = 5$. 57

ACKNOWLEDGEMENTS

First and foremost, I would like to thank Prof. Ricardo Carretero who so graciously took time out of his busy schedule to give me extensive guidance, and who, along with P. G. Kevrekidis and Q. E. Hoq, formulated the main idea for the theoretical methodology. I would also like to thank the other two members of the thesis committee, Profs. Michael Bromley and Peter Blomgren for their time in reviewing this thesis, and for their course instruction, much of which was vital to key methods used in this work. I also wish to acknowledge the Computational Science Research Center for their assistance and generous financial support. Last but certainly not least, I would like to thank my wife Molly for her great patience, understanding and support throughout the writing of this thesis.

CHAPTER 1

INTRODUCTION

We wish to study azimuthal modulational instability (MI) of vortex solutions to the two-dimensional Nonlinear Schrödinger Equation (NLS). We first introduce the NLS, and discuss two examples of physical systems that it describes. We then describe what vortex solutions to the NLS are, with their physical meaning in each application, and explain what the MI of the vortices refer to. Our motivation and purpose for the study of MI is given, along with a summary of the procedures that will be used.

1.1 BACKGROUND AND MOTIVATION

The NLS has been used to describe a very large variety of physical systems which exhibit nonlinear dynamics. This is because the NLS is the lowest order (cubic) nonlinear partial differential equation (PDE) that models the propagation of modulated waves. There are two main classes of NLS, depending on the sign of the nonlinearity. These are the focusing (or attracting), and the defocusing (or repulsive) cases. Which case to use depends on parameters in the physical system being described. The dimensionality of the NLS being used is also dependent on the physical problem.

Two interesting systems described by the NLS that our study is relevant to are Bose-Einstein Condensates (BECs), and light propagation in nonlinear crystals. In either application, the modulus squared of the wave function is what is observable in the system, as will be discussed.

A BEC is a super cold (on the order of $10^{-8}K$) collection of $10^3 - 10^6$ atoms which have predominantly condensed into the same quantum state, and therefore behaves like one large macroscopic atom. Its dynamics can be described (through a mean-field approach) by a variant of the NLS called the Gross-Pitaevskii (GP) equation. The GP equation is basically a NLS with an external potential term. The external potential term is necessary because in order to contain the condensation of the BEC, one needs to constantly apply an external potential which acts as a trap. The GP equation for a three-dimensional BEC as described in Ref. [1] is defined as:

$$i\hbar\Psi_t + \frac{\hbar^2}{2m_a}\nabla^2\Psi + V_{\text{ext}}(\mathbf{r})\Psi + \frac{4\pi\hbar^2 a_0}{m_a}|\Psi|^2\Psi, \tag{1.1}$$

where $\hbar$ is the reduced Planck constant, m_a is the mass of one of the atoms in the condensate, $V_{\text{ext}}(\mathbf{r})$ is the external potential function, $\nabla^2\Psi$ is the three-dimensional Laplacian, and a_0 is the s-wave scattering length. For a focusing case, $a_0 < 0$, while in a defocusing case, $a_0 > 0$.

The modulus squared of the wave function, $|\Psi|^2$, represents the density of the atoms in the condensate. Even though we do not analyze the GP equation directly, the MI results we find for vortices in the NLS are relevant to BECs, since the methodology we implement can easily incorporate the external potential term.

In BECs, a focusing nonlinearity has the physical meaning that the particles in the condensate will be attracted to one another in near-collisions. This can cause the BEC to collapse into itself, which in turn increases the kinetic energy of the particles, and leads to an 'explosive' destruction of the BEC dubbed a 'Bosenova' [2]. In the defocusing case, the particles in near-collision repel each other, in which case the BEC tries to expand. This is prevented by an external magnetic trap.

Although BECs are three-dimensional objects, by increasing the strength of the external trap in one transverse direction, one can form the BEC into a quasi-two-dimensional disk or even a quasi-one-dimensional cigar-shaped condensate in the case of two strong transverse directions [3]. Each of these situations can be described using appropriate forms of the two-dimensional and one-dimensional GP equations, and can exhibit very different dynamics. For example, for the focusing case, a three-dimensional BEC will always collapse, while a quasi-one-dimensional one will never collapse, even though it exhibits MI [3]. The critical case, is the quasi-two-dimensional disk shaped BEC, which can collapse if the amount of atoms in the condensate is above a critical threshold. It is in this quasi-two dimensional case, that we find vortex solutions of the kind we are studying here [3].

Nonlinear crystals are crystals which exhibit a nonlinear optical response when light propagates through them. There are many different varieties of nonlinear crystals, each with different nonlinear effects. One such effect, called the Kerr effect, is when the refractive index of the light being propagated through the crystal is changed proportional to the intensity of the light. Propagation of light through a crystal exhibiting the Kerr effect can be modeled using the NLS, where the modulus squared of the wave function represents the intensity of the light. In such a case, a $(2+1)$-dimensional NLS is used, where the two dimensions of the wave function represent a cross-section of the crystal, while the propagation dimension (which represented time in the case of BECs) represents the direction of propagation:

$$2i\beta_0\Psi_z + \nabla^2\Psi + \beta_0^2\left(\frac{n_2}{n_0}\right)|\Psi|^2\Psi, \tag{1.2}$$

where z is the propagation direction, $\nabla^2\Psi$ is the two-dimensional Laplacian, and β_0 is the propagation constant. The parameters n_0 and n_2 form the index of refraction in the crystal as $n = n_0 + n_2|\Psi|^2$, where n_0 is the index of refraction of the crystal in the absence of light, and n_2 is the change in the index of refraction due to the intensity of the light present in the crystal [4].

In a nonlinear crystal, the defocusing case corresponds to a negative change in the refractive index of the crystal ($n_2 < 0$) which causes the light to defocus and spread out as it propagates through the crystal. The focusing case ($n_2 > 0$) corresponds to a positive change in the refractive index of the crystal, which acts to focus the light, increasing its intensity. This focusing increases until the crystal is saturated, an effect which is not accounted for in Eq. (1.2), but can be modeled using an NLS with a saturable nonlinearity [5]. Despite this, our MI study presented here is still directly relevant because the saturation effects do not become important until the growth in intensity is very strong, and our study is limited to small perturbations.

In the two-dimensional NLS, there exists an interesting family of solutions called vortices. Vortices are ring-shaped structures which have a rotational periodic angular phase associated with them. This phase rotates around in time (or propagation length), giving the system angular momentum. A property of the vortex is its topological charge, denoted as m, which indicates how many periods there are in the angular phase. For $|m| > 0$, the wave function at the center of the vortex becomes identically zero, causing the ring-like shape. An example of a vortex for the focusing NLS with charge $m = 3$ is shown in Fig. 1.1.

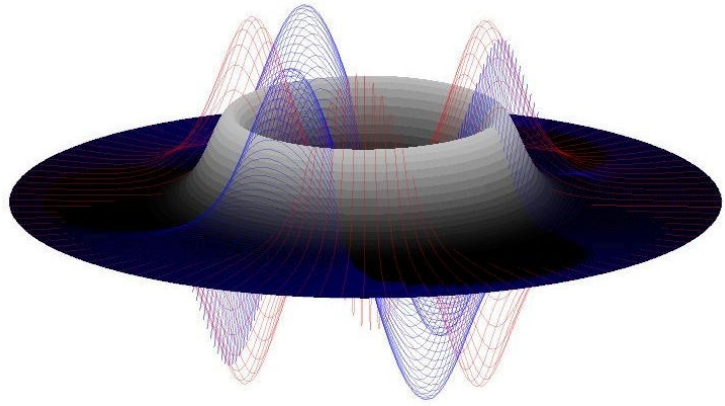

Figure 1.1. An example of a simulated vortex solution to the two-dimensional focusing NLS. The blue and red mesh correspond to the real and imaginary parts of the wave function respectively, which have three periods in the angular phase corresponding to a vortex charge of $m = 3$. The gray volume corresponds to the modulus squared of the wave function, which is the physically observable quantity of the system.

In BECs, two-dimensional vortex solutions of the kind depicted in Fig. 1.1 correspond to a quasi-two-dimensional BEC which has been 'stirred' as described in Ref. [6], forming a spinning ring-shaped BEC as depicted in Fig. 1.2.

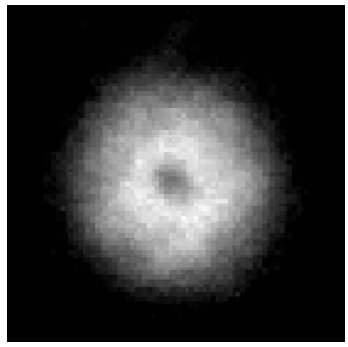

Figure 1.2. A transverse absorption image of a quasi-two-dimensional BEC which has been stirred into a vortex with a laser beam. Source: K. W. Madison, F. C., W. Wohileben and J. Dalibard. Vortex formation in a stirred Bose-Einstein condensate. *Physical Review Letters*, 84 (2000) 807.

In nonlinear crystals, vortex solutions correspond to the propagation of optical vortices through the crystal. Optical vortices occur when the electric field envelope of light exhibits a phase singularity, where the phase of the field is rotated about the axis of propagation m number of times per wavelength for a vortex of charge $|m|$. Optical vortices can exist in free space, as well as linear optical media, where the vortex ring defracts as it propagates. In a focusing nonlinear crystal, such vortices propagate without changing their shape, that is, until modulational instability breaks up the vortex into filaments as will be discussed shortly [7]. Some examples of optical vortices of different charges are shown in Fig. 1.3 [8].

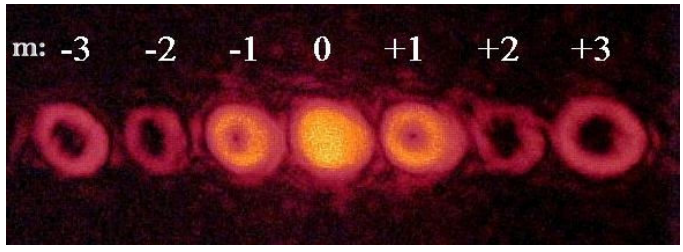

Figure 1.3. Projection of optical vortices of different topological charges onto a dark surface formed by passing a laser beam through a specialized fork grating. Photo courtesy of A. Hansen, Stony Brook University. Source: Wikipedia. Opticalvortices: http://en.wikipedia.org/wiki/image:opticalvortices.jpg, 2004.

In any application, the vortex solution of the NLS in the focusing case is modulationally unstable in the azimuthal direction. This means that a vortex will exhibit exponential growth of azimuthal modes, where each mode (denoted as an integer value K) has its own growth rate. This leads to the destruction of the vortex into $|K|$ number of filaments. Because the MI is on the azimuthal direction, the natural modes are periodic Fourier modes. An example of such a 'blow up' is depicted in Fig. 1.4.

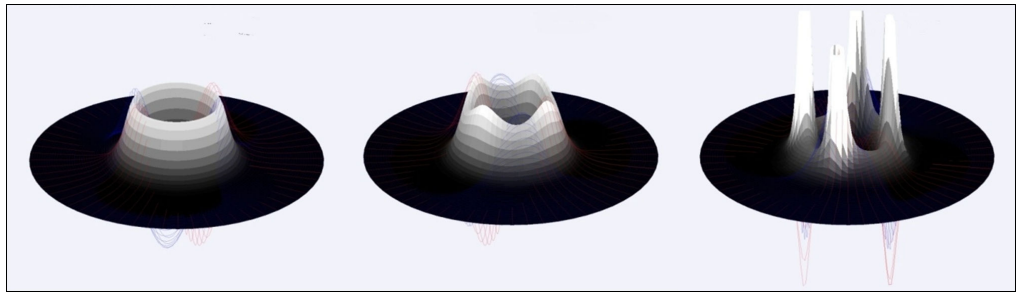

Figure 1.4. Simulated exponential 'blow up' of a mode $K = 4$ perturbation into filaments of a two-dimensional vortex solution to the NLS of charge $m = 2$ due to azimuthal modulational instability. The red, blue and gray regions are as described in Fig. 1.1. Left: The vortex in a steady-state. Middle: The vortex exhibiting growth of a mode $K = 4$ perturbation. Right: Resulting filaments after the 'blow up' of the perturbation.

There are many extensions to the classic NLS, including external potentials (as in the GP equation above), nonlocal interactions [9], higher-order nonlinearities [5], etc. which in theory might damp or even eliminate the MI of vortices. In order to know whether such extensions would actually damp the MI of vortices, one needs a general methodology for the study of MI, which would be able to predict the critical mode, below which all modes are unstable. Predicting the growth rates of the unstable modes would also be useful so that one would know how long or far a vortex could propagate before the MI breaks it up into filaments. The methodology for the study of MI should be general enough to be able to incorporate the extensions to the NLS mentioned above.

1.2 PURPOSE

Our purpose here is to formulate and test an expandable method of studying the azimuthal modulational instability of vortex solutions to the NLS. We wish to be able to predict the growth rates of the unstable modes, and predict the critical mode, below which all modes are unstable. By demonstrating the reliability of the method used on the non-dimensionalized NLS through numerical simulations, we hope to better understand the

MI of vortices, as well as introduce a new tool for their study. One example of extending the method, that of incorporating a nonlocal nonlinearity to the NLS, is given in Chap. 8.

1.3 PROCEDURE

The procedure used here was first formulated by Carretero, *et al* in the in-progress paper of Ref. [10]. We view the steady-state vortex solution as separable into a time-dependent azimuthal function and a frozen radial function. This ansatz is then inserted into the Lagrangian functional of the NLS in question, in which case the integrals over the radial direction become constants. Then, the variational derivative of the Lagrangian yields a quasi-one dimensional azimuthal equation of motion. A perturbation method and linear stability analysis is then done on this equation to predict the MI critical mode and growth rates for each mode.

In order to perform this methodology, one must obtain the radial profile of a steady-state (in terms of the modulus squared) vortex, which in general does not have an analytic solution. To do this, we apply a variational approach (VA) to obtain analytic expressions resembling the true radial profile, and then we use this as an initial guess to a nonlinear numerical optimization routine to obtain the true steady-state radial profile.

Once the theoretical predictions are made from the steady-state radial profile, it is fed as an initial condition into a full two-dimensional simulation of the NLS using a finite difference scheme on a polar grid. This initial condition is perturbed with the modes under consideration, and the growth rates are calculated for comparison to the theory.

We show that overall the predictions of the growth rates of each mode, as well as the prediction for the critical mode match the numerical simulations very well. The growth rates are generally predicted to be within around 8% of those recored in the numerical simulations, and the critical mode is predicted either exact, or one mode off. We then note the possible sources for these errors, and ways to minimize them.

CHAPTER 2

THE MODEL

Here, we formulate our model by using the action functional of the two-dimensional NLS to derive a quasi-one-dimensional PDE describing the evolution of the azimuthal part of a separable radially-frozen solution.

2.1 TWO-DIMENSIONAL NONLINEAR SCHRÖDINGER EQUATION

We have already shown two examples of NLS-type equations in Eqs. (1.1) and (1.2). In general, we can write a two-dimensional NLS-type equation (without an external potential) as:

$$ia\frac{\partial\phi}{\partial\tau} + b\left(\frac{\partial^2\phi}{\partial X^2} + \frac{\partial^2\phi}{\partial Y^2}\right) + s|c|\,|\phi|^2\phi = 0, \tag{2.1}$$

where ϕ is the wave function, τ is the propagation dimension, X and Y are the transverse directions, a, b, and c are parameters determined by the physical system, and $s = \pm 1$ is the sign of c which denotes a focusing or defocusing case respectively. We can non-dimensionalize Eq. (2.1) without loss of generality by applying the following rescalings:

$$\begin{aligned} \phi &= \alpha\Psi, \qquad & X &= \beta x, \\ \tau &= \gamma t, \qquad & Y &= \beta y, \end{aligned} \tag{2.2}$$

which, after dividing through Eq. (2.1) by α, yields:

$$ia\frac{1}{\gamma}\frac{\partial\Psi}{\partial t} + b\frac{1}{\beta^2}\left(\frac{\partial^2\Psi}{\partial x^2} + \frac{\partial^2\Psi}{\partial y^2}\right) + s|c|\alpha^2\,|\Psi|^2\Psi = 0. \tag{2.3}$$

If we set our rescalings to be:

$$\gamma = a, \qquad \beta^2 = b, \qquad \alpha = \frac{1}{\sqrt{|c|}}, \tag{2.4}$$

we obtain the non-dimensionalized NLS:

$$i\Psi_t + \nabla^2\Psi + s\,|\Psi|^2\Psi = 0, \tag{2.5}$$

where $\nabla^2\Psi$ is the two-dimensional Laplacian of the wave function, and as above, $s = +1$ denotes the focusing case, while $s = -1$ is the defocusing case. Therefore, we see that we can use Eq. (2.5) to study MI of vortices without loosing any generality to physical systems which

use the NLS of the form of Eq. (2.1). Also, although we will only deal with the focusing case ($s = +1$), we leave s in our equations to maintain generality. The natural coordinate system for studying the MI of vortices is polar, where the Laplacian takes on the form:

$$\nabla^2\Psi = \frac{1}{r}\frac{\partial}{\partial r}\left(r\frac{\partial\Psi}{\partial r}\right) + \frac{1}{r^2}\frac{\partial^2\Psi}{\partial\theta^2}.$$

As described in Ref. [11], we note that in any conservative dynamical system, we can define the Lagrangian, L, as $L = T - V$ where T is the total kinetic energy of the system at a given moment of time, and V is the total potential energy.

The Hamiltonian principle in mechanics states that the first variation of the time integral of the Lagrangian (referred to as the action functional of the system) must be stationary (i.e. 0). If we define the action functional as S, then we must have:

$$\delta S = \delta \int_{t_1}^{t_2} L\, dt = 0,$$

where δ denotes the variational derivative.

Using the action functional, one can derive equations of motion for a system. This is done by formulating an expression for L and, by performing the variational derivative, obtaining the equation of motion. In our case, we first look for an L which will lead us back to the NLS we started from. Then, in the next section, we will use that Lagrangian to derive our azimuthal equation of motion which we will use to study the MI of vortices.

In our problem, we can define the action functional of Eq. (2.5) as:

$$S = \int_0^{\infty} L\, dt, \tag{2.6}$$

where the Lagrangian, L is written as:

$$L = \int_0^{2\pi}\int_0^{\infty} \mathcal{L}\, r\, dr\, d\theta, \tag{2.7}$$

where we define (as depicted in Ref. [12]) the Lagrangian Density, $\mathcal{L}$ as:

$$\mathcal{L} = \frac{i}{2}\left(\Psi\Psi_t^* - \Psi^*\Psi_t\right) + |\Psi_r|^2 + \left|\frac{1}{r}\Psi_\theta\right|^2 - \frac{s}{2}|\Psi|^4. \tag{2.8}$$

We now insert a separable solution to obtain an azimuthal equation of motion.

2.2 AZIMUTHAL EQUATION OF MOTION

In order to find the azimuthal equation of motion, we assume a separable solution with a steady-state radial profile:

$$\Psi(r,\theta,t) = f(r)\,A(\theta,t), \tag{2.9}$$

where all of the phase components of the solution are contained in A, and therefore $f(r) \in \Re$. For two-dimensional vortices, we must be careful in making this assumption. Although a steady-state vortex is radially symmetric, and therefore separable, the dynamics of the vortex after being perturbed by a small complex azimuthal perturbation is not. This is evident if we look at some (numerically derived) eigenmodes of the vortex solutions as shown in Fig 2.1.

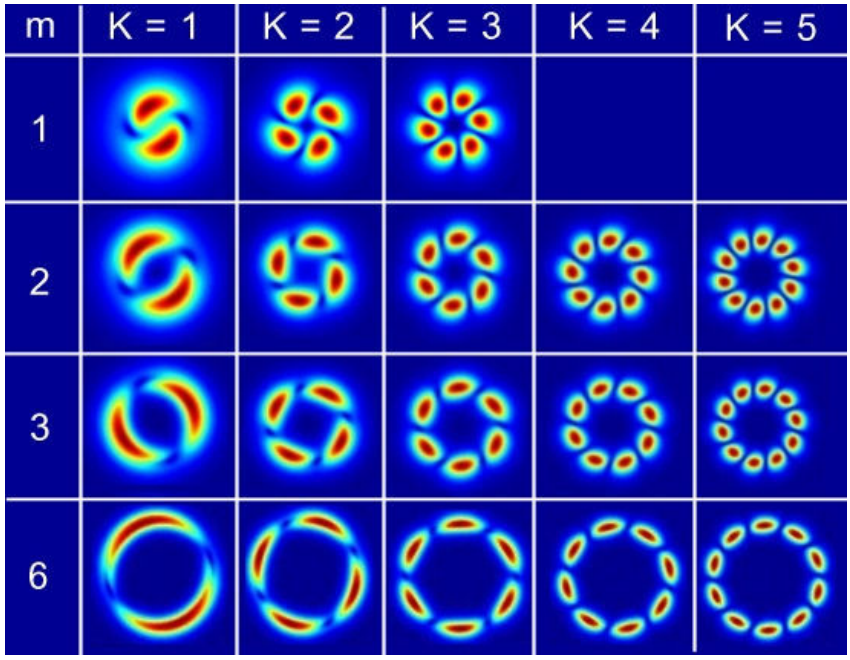

Figure 2.1. Depiction of the modulus squared of numerically derived unstable eigenmodes of vortices in the two-dimensional focusing NLS of charges $m = 1, 2, 3,$ and 6 for modes $K = 1, ..., 5$ (the vortex of charge $m = 1$ does not have unstable modes past $K = 3$). It is obvious from the panels that the eigenmodes are not completely separable as assumed in Eq. (2.9), but can be reasonably approximated by such a separable solution. We also see that for higher charges and higher mode numbers, the eigenmodes appear to become more separable, and thus the approximation of a separable solution becomes more accurate. The unpublished plots depicted here were computed numerically by Prof. Carretero on a Cartesian grid of 180×180 using a Newton's method to form the vortices, and numerically computing the Jacobian of the two-dimensional NLS to find the eigenmodes.

We see that the eigenmodes of the vortices are not separable, which means that there is a weak coupling of the radial and azimuthal directions. We also notice that the degree of coupling varies for different modes, and for different vortex charges. It appears that, generally, for higher vortex charges, the modes appear more separable. However, even for lower charges, assuming a separable solution is an acceptable approximation, since as we will show in Sec. 7.2, our growth rate predictions for each mode formed under such an approximation are close (usually within 10%) to the numerical simulation results. Also, our predictions for the critical mode are at most off by only one mode number. Therefore we are justified in using Eq. (2.9).

When Eq. (2.9) is inserted into Eq. (2.7), than since $f(r)$ is steady-state, or frozen, then all radial dependent integrals become constants. This allows us to transform the two-dimensional Lagrangian into a quasi-one dimensional (in θ) Lagrangian which can be used to find the equation of motion for $A(\theta, t)$. We use the term 'quasi-one-dimensional' because although it becomes a one-dimensional problem, the radial direction is not ignored, but shows itself in the values of the radial integral constants.

First, we insert Eq. (2.9) into the Lagrangian density:

$$\mathcal{L} = |f(r)|^2 \frac{i}{2}(AA_t^* - A^*A_t) + \left|\frac{df}{dr}A\right|^2 + \left|\frac{1}{r}f(r)A_\theta\right|^2 - |f(r)|^4 \frac{s}{2}|A|^4$$

Now we evaluate the radial integrals of the Lagrangian to obtain our quasi-one-dimensional Lagrangian:

$$L_{\text{1D}} = \int_0^{2\pi} \mathcal{L}_{\text{1D}}\, d\theta,$$

where

$$\mathcal{L}_{\text{1D}} = \frac{i}{2}C_1(AA_t^* - A^*A_t) + C_2|A|^2 + C_3|A_\theta|^2 - \frac{s}{2}C_4|A|^4, \tag{2.10}$$

where

$$C_1 = \int_0^\infty |f(r)|^2\, r\, dr, \qquad C_2 = \int_0^\infty \left|\frac{df}{dr}\right|^2 r\, dr, \tag{2.11}$$
$$C_3 = \int_0^\infty \frac{1}{r^2}|f(r)|^2\, r\, dr, \qquad C_4 = \int_0^\infty |f(r)|^4\, r\, dr,$$

We evaluate the variational derivative of the action functional as shown in Ref. [12], which in this case takes the form:

$$\frac{\delta S}{\delta A^*} = \frac{\partial}{\partial t}\frac{\partial \mathcal{L}_{\text{1D}}}{\partial [A_t^*]} + \frac{\partial}{\partial \theta}\frac{\partial \mathcal{L}_{\text{1D}}}{\partial [A_\theta^*]} - \frac{\partial \mathcal{L}_{\text{1D}}}{\partial A^*} = 0. \tag{2.12}$$

Inserting Eq. (2.10) into Eq. (2.12) yields the evolution equation for $A(\theta, t)$:

$$i\, C_1 A_t = C_2 A - C_3 A_{\theta\theta} - s\, C_4 |A|^2 A. \tag{2.13}$$

We now have an equation of motion for the azimuthal direction of a separable solution to the two-dimensional NLS. This equation is quasi-one-dimensional, in that although it is a one-dimensional equation, it incorporates information from the radial direction in the C-constants. Such an azimuthal equation has not been derived in this manner as far as we know. This equation is very useful, in that we can now apply the standard tools for analyzing the stability of MI of a one-dimensional NLS (as in Ref. [13]) to our two-dimensional problem.

CHAPTER 3

STABILITY ANALYSIS

In this chapter we use a perturbation technique and discrete Fourier series expansions to obtain amplitude equations for each azimuthal mode of a complex perturbation to a steady-state solution of Eq. (2.13). Then, to study the MI of Eq. (2.13), we look at the linear stability analysis of the amplitude equations of the perturbation in order to predict the critical mode (below which the system is unstable), and also to predict the growth rates of each unstable mode.

3.1 SIMPLIFICATIONS AND DISPERSION RELATION

Before starting the perturbation method, we first make two simplifications to Eq. (2.13). The first simplification is to apply the gauge transformation:

$$A \to A \exp\left(-i\frac{C_2}{C_1}t\right), \tag{3.1}$$

which eliminates the linear term proportional to A, and does not affect the growth rates of the Fourier modes, or the critical mode because we are simply adding a phase rotation.

The next simplification we make is to rescale time as:

$$t \to \frac{C_3}{C_1}\,t, \tag{3.2}$$

which eliminates C_1 from the equation, and moves the other constants to the nonlinear term. This rescaling does not affect the critical mode (since we have the same dynamics, only evolving faster or slower in time), however it does change the growth rates of each mode, and therefore must be taken into account later on. Applying these simplifications yields:

$$iA_t = -A_{\theta\theta} - s\frac{C_4}{C_3}|A|^2 A, \tag{3.3}$$

which is simply the one dimensional NLS with a specific constant prefactor multiplying to the nonlinearity.

For the stability analysis, we assume an azimuthal 'plane wave' solution to Eq. (3.3):

$$A(\theta, t) = e^{i(m\theta + \Omega' t)}, \tag{3.4}$$

where m is the topological charge of the vortex, and Ω' is the frequency of rotation of the complex phase. We use the notation Ω' so as not to confuse this frequency with that of the full

two dimensional system which would include the terms in the gauge transformation. The amplitude of the plane wave does not appear as an explicit term because it is absorbed into the $f(r)$ of Eq. (2.9).

If we insert Eq. (3.4) into equation Eq. (3.3), we get the following dispersion relation:

$$\Omega^{'} = -m^2 + s\frac{C_4}{C_3}, \tag{3.5}$$

which we can now use for a perturbation method.

3.2 PERTURBATION METHOD

To study stability of different modes, we use the technique from Ref. [13] to derive equations of motion for a complex perturbation. Specifically, we wish to derive the amplitude equations for each perturbed Fourier mode.

We start by perturbing Eq. (3.4) with a complex, time-dependent perturbation of the form:

$$A(\theta, t) = (1 + u(\theta, t) + iv(\theta, t))\ e^{i(m\theta + \Omega^{'} t)}, \tag{3.6}$$

where $|u|, |v| \ll 1$. Inserting this into Eq. (3.3), and using Eq. (3.5), we can separate the result into real and imaginary parts to get a system of coupled PDEs describing the evolution of the perturbation $u(\theta, t)$ and $v(\theta, t)$:

$$u_t = -2mu_\theta - v_{\theta\theta} - \left[s\tfrac{C_4}{C_3}\left(2uv + u^2v + v^3\right)\right],$$

$$v_t = -2mv_\theta + u_{\theta\theta} + 2s\tfrac{C_4}{C_3}\,u + \left[s\tfrac{C_4}{C_3}\left(v^2 + 3u^2 + v^2u + u^3\right)\right].$$

To simplify the analysis, we can set ourselves on a rotating frame with angular velocity of $2m$ by rescaling time as:

$$\tau = t + \frac{1}{2m}\,\theta,$$

in which case, by the chain rule:

$$\frac{\partial u}{\partial t} = \frac{\partial u}{\partial \tau}\frac{d\tau}{dt} + \frac{\partial u}{\partial \theta}\frac{d\theta}{dt} = \frac{\partial u}{\partial \tau} - 2m\frac{\partial u}{\partial \theta},$$

$$\frac{\partial v}{\partial t} = \frac{\partial v}{\partial \tau}\frac{d\tau}{dt} + \frac{\partial v}{\partial \theta}\frac{d\theta}{dt} = \frac{\partial v}{\partial \tau} - 2m\frac{\partial v}{\partial \theta}.$$

If we rename τ as t, we now have:

$$\begin{aligned} u_t &= -v_{\theta\theta} - \left[s\tfrac{C_4}{C_3}\left(2uv + u^2v + v^3\right)\right], \\ v_t &= u_{\theta\theta} + 2s\tfrac{C_4}{C_3}\,u + \left[s\tfrac{C_4}{C_3}\left(v^2 + 3u^2 + v^2u + u^3\right)\right]. \end{aligned} \tag{3.7}$$

In order to study MI, we need to obtain amplitude equations for the azimuthal modes. To do this, we first expand u and v in a discrete Fourier series:

$$u(\theta,t)=\frac{1}{2\pi}\sum_{K=-\infty}^{\infty}\hat{u}(K,t)e^{-iK\theta},\qquad v(\theta,t)=\frac{1}{2\pi}\sum_{K=-\infty}^{\infty}\hat{v}(K,t)e^{-iK\theta},\tag{3.8}$$

where K is the mode number and where the amplitudes for each mode are given by:

$$\hat{u}(K,t)=\int_0^{2\pi}u(\theta,t)\,e^{iK\theta}\,d\theta,\qquad \hat{v}(K,t)=\int_0^{2\pi}v(\theta,t)\,e^{iK\theta}\,d\theta.\tag{3.9}$$

Applying these to Eq. (3.7) yields two coupled nonlinear ODEs describing the dynamics for the amplitudes of u and v for each mode:

$$\begin{aligned}\hat{u}_t&=K^2\hat{v}-\left[s\tfrac{C_4}{C_3}\left(2\hat{u}*\hat{v}+\hat{u}*\hat{u}*\hat{v}+\hat{v}*\hat{v}*\hat{v}\right)\right],\\ \hat{v}_t&=\left(2s\tfrac{C_4}{C_3}-K^2\right)\hat{u}+\left[s\tfrac{C_4}{C_3}\left(\hat{v}*\hat{v}+3\hat{u}*\hat{u}+\hat{v}*\hat{v}*\hat{u}+\hat{u}*\hat{u}*\hat{u}\right)\right],\end{aligned}\tag{3.10}$$

where now the nonlinear terms become convolution terms defined generally as:

$$\hat{a}*\hat{b}\,(K,t)=\sum_{K'=-\infty}^{\infty}\hat{a}(K',t)\,\hat{b}(K-K',t).$$

With Eq. (3.10), we can study the stability of the amplitudes of any given perturbation mode.

3.3 Linear Stability Analysis

Since we want to study the MI of small perturbations, we are not interested in the long-term dynamics of Eq. (3.10). Rather, we want to know whether very small perturbations of different azimuthal modes will be unstable and start to grow exponentially. Since $|\hat{u}|$ and $|\hat{v}|$ are very small, we can linearize the system by ignoring the higher order convolution terms. This allows us to ignore any inter-mode interactions, and focus on each the stability of each perturbed mode one at a time.

We can write the linearized system of Eq. (3.10) in matrix form as:

$$\begin{bmatrix}\hat{u}_t\\ \\ \hat{v}_t\end{bmatrix}=\begin{bmatrix}0 & K^2\\ \\ \left(2s\frac{C_4}{C_3}-K^2\right) & 0\end{bmatrix}\begin{bmatrix}\hat{u}\\ \\ \hat{v}\end{bmatrix}.\tag{3.11}$$

The eigenvalues are:

$$\lambda_{1/2}=\pm\sqrt{K^2\left(2s\frac{C_4}{C_3}-K^2\right)}.$$

We notice that for a defocusing nonlinearity ($s = -1$), since $C_4/C_3 \geq 0$, the eigenvalues are purely imaginary and therefore all small perturbations are neutrally stable. For our focusing case ($s = +1$), there is a bifurcation at a critical value of K, in which the fixed point changes from a saddle point to a neutrally stable center as shown in Fig. 3.1. This means that the amplitude of a perturbation of any integer mode above the critical value should simply oscillate, and any mode below should be unstable and grow exponentially. We define this critical value as:

$$K_{\text{crit}} \equiv \sqrt{2s\frac{C_4}{C_3}}. \tag{3.12}$$

To predict the actual growth rates for the perturbation of each mode from the eigenvalues, the time rescaling of Eq. (3.2) needs to be taken into account, in which case the growth rates (in terms of K_{crit}) are:

$$\lambda_{1/2} = \pm\frac{C_3}{C_1}\sqrt{K^2\left(K_{\text{crit}}^2 - K^2\right)}. \tag{3.13}$$

The normalized eigenvectors, which become important later in the initial conditions for the

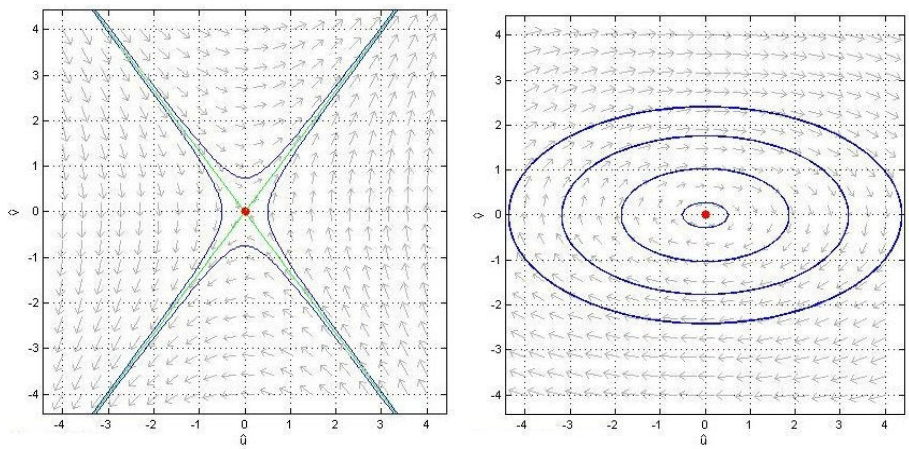

Figure 3.1. Phase portrait of Eq. (3.11) for $K_{\text{crit}} = 5$. The axis represent the value of the height of the real ($\hat{u}$) and imaginary ($\hat{v}$) parts of a perturbation of mode number K. Left: The phase portrait for $K = 3$ showing the stable and unstable manifolds of the saddle point, along with a few sample trajectories. As can be seen, any initial condition will become attracted to the unstable manifold and the amplitudes will exponentially increase. Right: The phase portrait for $K = 6$ showing the neutrally stable center point with some sample trajectories. Any initial perturbation simply oscillates in height.

numerical simulations, are:

$$\mathbf{v}_{1/2} = \begin{bmatrix} \pm\frac{K}{K_{\text{crit}}} \\ \\ \sqrt{1-\left(\frac{K}{K_{\text{crit}}}\right)^2} \end{bmatrix} \tag{3.14}$$

Now that we have our growth rates and critical mode defined, we need to find a steady-state vortex solution in order to calculate values for the C-constants, and use it as an initial condition for our simulations.

CHAPTER 4

FINDING STEADY-STATE VORTEX SOLUTIONS

Explicit solutions for two dimensional steady-state vortices of the NLS are not available. Therefore, in order to find a solution, we use a variational approach (VA) to get a reasonable ansatz, and then use that ansatz as an initial condition to a nonlinear equation optimization routine which finds the numerically exact steady-state profile. We also find using the VA, an analytic asymptotic solution for vortices, which seems to converge to the true solution as $m \to \infty$. Finally, we show that the solutions form a family of solutions that depend only on m and Ω. For any choice of m, different choices for Ω are simply rescalings of time and space for one single solution, and thus all have the same K_{crit}.

4.1 VARIATIONAL APPROACH

To perform the VA, we use the technique described in Ref. [12]. We insert a vortex ansatz with variable parameters into the Lagrangian of the NLS, and use the Euler-Lagrange equations to find the 'best' values for the parameters. We start with a general, separable, steady-state solution:

$$\Psi(r,\theta,t) = f(r)e^{i(m\theta+\Omega t)}, \tag{4.1}$$

where $f(r)$ is the steady-state radial profile which we want to find. Inserting this solution into the Lagrangian density of the NLS yields:

$$\mathcal{L}(r,\theta) = \left(\Omega + \frac{m^2}{r^2}\right)|f(r)|^2 + \left|\frac{df}{dr}\right|^2 - \frac{s}{2}|f(r)|^4. \tag{4.2}$$

We want to choose a formulation for $f(r)$ that is close to the true vortex profile. We use the ansatz from Ref. [14] because it closely matches a vortex profile of charge $m = 1$, and can be integrated explicitly (since it is a Gaussian) without too much difficulty. This ansatz is:

$$f(r) = B\,r\exp\left(\frac{-r^2}{2\sigma^2}\right), \tag{4.3}$$

where B, and σ are the parameters that we want to find. Using this ansatz in Eq. (4.2), yields the Lagrangian:

$$\begin{aligned} L &= \int_0^{2\pi}\int_0^{\infty} B^2 e^{-\frac{r^2}{\sigma^2}}\left[(m+1) + r^2\left(\Omega - \frac{2}{\sigma^2}\right) + r^4\left(\frac{1}{\sigma^4} - \frac{sB^2}{2}e^{-\frac{r^2}{\sigma^2}}\right)\right] r\,dr\,d\theta \\ &= \pi B^2\sigma^2\left[(m+1) - \left(\frac{s}{8}B^2\sigma^2 - \Omega\right)\sigma^2\right]. \end{aligned} \tag{4.4}$$

The Euler-Lagrange equations for the steady-state solution take the form:

$$\frac{\partial L}{\partial B} = 0, \qquad \frac{\partial L}{\partial \sigma} = 0, \tag{4.5}$$

which when evaluated, gives:

$$2\pi B\sigma^2 \left[(m+1) - \left(\frac{s}{4}B^2\sigma^2 - \Omega\right)\sigma^2\right] = 0,$$
$$2\pi B^2\sigma \left[(m+1) - \left(\frac{3s}{8}B^2\sigma^2 - 2\Omega\right)\sigma^2\right] = 0.$$

We need to solve these two equations for the parameters B and σ. There are six pairs of solutions. Two of them are trivial. From the remaining four, the fact that we must have $B > 0$ and $\sigma > 0$ leaves us with only one possible non-trivial solution pair:

$$B = \Omega\sqrt{\frac{8}{s(m+1)}}, \qquad \sigma^2 = \frac{m+1}{\Omega}. \tag{4.6}$$

We see that for every choice of Ω, there is only one VA ansatz for each charge. Substituting Eq. (4.6) into Eq. (4.3) gives the radial VA profile (which we denote VA1):

$$f(r; m, \Omega) = r\,\Omega\sqrt{\frac{8}{s(m+1)}}\exp\left(\frac{-\Omega\, r^2}{2(m+1)}\right). \tag{4.7}$$

Now that we have our VA profile, we can use a numerical optimization routine to refine it into the numerically exact steady-state radial profile.

4.2 Numerical Optimization

In this section, we describe our implementation of a nonlinear equation optimization routine and use it to refine Eq. (4.7) into a numerically 'exact' solution.

We set up the problem by inserting the following separable steady-state solution into Eq. (2.5):

$$\Psi(r, \theta, t) = f(r)\, e^{im\theta}\, e^{i\Omega t}, \tag{4.8}$$

which produces the following ODE (remembering that $f(r) \in \Re$):

$$-\left(\Omega + \frac{m^2}{r^2}\right) f(r) + \frac{1}{r}\frac{\partial}{\partial r}\left(r\frac{\partial f}{\partial r}\right) + s\, f(r)^3 = 0. \tag{4.9}$$

We can discretize the radial direction as shown in Fig. 4.1. Now using a second order finite difference approximation, we can write Eq. (4.9) as the vector function:

$$\vec{F}(\vec{f}(r)) = -\left(\Omega + \frac{m^2}{r_i^2}\right) f_i + \frac{1}{r_i}\frac{1}{\Delta r}\left(r_{i+\frac{1}{2}}\frac{f_{i+1} - f_i}{\Delta r} - r_{i-\frac{1}{2}}\frac{f_i - f_{i-1}}{\Delta r}\right) + f_i^3 = \vec{0}, \tag{4.10}$$

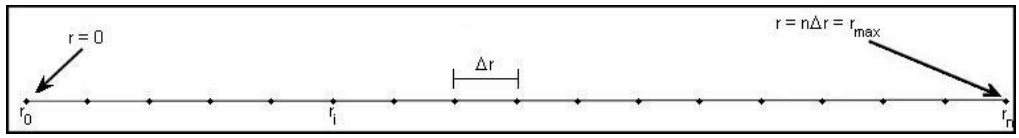

Figure 4.1. Discretization of radial direction. r_0 **is the center point of the disk at** $r = 0$**. The grid spacing is represented by** Δr**. The maximum radius of the disk is given by** $r_{\mathbf{max}} = n\Delta r$ **where** n **is the total number of radial grid points.**

where Δr is the grid spacing length, $r_i = i\Delta r$, and $f_i = f(r_i)$.

What we want is a radial profile input vector (call it $\vec{f}^*$) which minimizes $\vec{F}$ to a specific minimum value, i.e. $\vec{0}$. Thus, the problem can be looked at as a minimization problem, which can be solved using numerical optimization techniques taken from Ref. [15].

In any optimization algorithm, the idea is to iterate a trial solution, denoted $\vec{f}_0$, of a function, denoted $M(f)$, through the space of the problem towards a local minimum solution, denoted $\vec{f}^*$, by taking carefully selected steps of specific direction and length:

$$\vec{f}_{k+1} = \vec{f}_k + \alpha_k \vec{p}_k,$$

where α_k is the step length for step number k, and p_k is the step direction. The goal is to lead quickly to a local minimum of M, thus finding the minimized solution, $\vec{f}^*$. In other words, we want $\nabla M(f^*) = 0$, where ∇M denotes the gradient of the function. To illustrate this process, we show an example for an $M : \Re^2 \to \Re$ function in Fig. 4.2.

Given a step direction, one needs to find an appropriate step size. To do this, we use a line search. A line search takes the step direction, and ideally finds the exact minimum of the function along that direction, and chooses the step length accordingly:

$$\min_{\alpha>0} M(\vec{f}_k + \alpha\vec{p}_k) \to \alpha_k.$$

In practice however, an inexact line search is used, where instead of finding the exact minimum along the step direction, a step length is determined which satisfies some minimum 'progress' conditions, the most common of which are called the Wolfe conditions:

$$\begin{aligned} M(f_k + \alpha_k p_k) &\leq M(f_k) + c_1\alpha_k \nabla M_k^T p_k, \\ \nabla M(f_k + \alpha_k p_k)^T p_k &\geq c_2 \nabla M_k^T p_k, \end{aligned} \tag{4.11}$$

where $0 < c_1 < c_2 < 1$ [15]. To find the inexact α_k, we use a backtracking search. This is where we attempt a 'large' step length (which, for the Newton methods described below is the full step of length 1), test the Wolfe conditions, and if our current step length does not satisfy them, we lower α_k by a constant factor, $\alpha_k = \rho\alpha_k$, where $\rho \in (0, 1)$. This method guarantees that we will find a satisfactory step length in each iteration. It also has the benefit that its

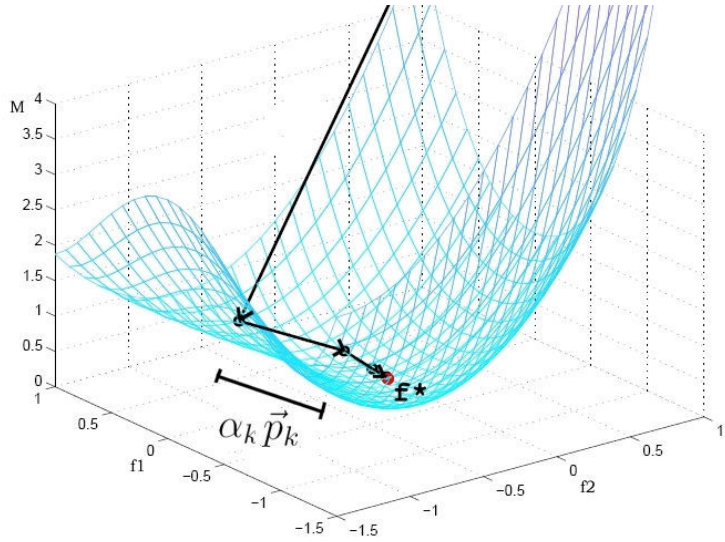

Figure 4.2. An example of a numerical optimization process for the function $M(\vec{f}) = (f_1 + f_2^2)^2 + 0.5(f_1^2 + f_2^2)$. The blue mesh is the function M, and the black arrows represent individual iteration steps of the trial solution in the direction p_k with step length α_k, where k is the step number. The step direction is chosen by Newton's method, and the step length by a backtracking line search. The steps lead to the minimum solution of $\vec{f}^* = [0, 0]$.

design eliminates the need for testing both Wolfe conditions, allowing us to only test the first condition, while the second condition is implicitly guaranteed to be true as well (see Ref. [15] for details).

When optimizing a function $M : \Re^n \to \Re$, there are different strategies in choosing p_k. A common way to choose p_k is the Newton step $p_k = -\nabla^2 M_k^{-1} \nabla M_k$ where $\nabla^2 M_k$ is the full Hessian of M, which when combined with the line search described above, converges quadratically. However, for our problem we have a function $F : \Re^n \to \Re^n$, in which case, the Newton step is actually easier to compute, and only requires the Jacobian of F and not the full Hessian:

$$p_k = -J_k^{-1} \vec{F}(f_k),$$

where $J_k \equiv J(f_k)$ is the Jacobian.

However, in order to use the line search, we need a $\Re^n \to \Re$ function so that we can compute the gradient in the Wolfe conditions, and also so we can set a stopping criteria for the overall method. In order to do this, we define a merit function, $M : \Re^n \to \Re$ as:

$$M(\vec{f}) = \frac{1}{2} \sum_{i=1}^{n} (F_i(\vec{f}))^2. \tag{4.12}$$

The gradient of M is then easily computed as:

$$\nabla M(\vec{f}) = J(\vec{f})^T \vec{F}(\vec{f}). \tag{4.13}$$

There is an important issue to take note of. As we have said above, typically in an optimization algorithm, we want to find a local minimum of M, i.e. $\nabla M = 0$, but we do not require $M(f^*)$ to take on any specific value (in fact, often times that value is what we want to find out!). However, in our problem, we need $\nabla M(f^*) = 0$ (so we can progress using the line search and know when we are at a minimum) but we also need to have the specific value for the minimum to be $M(\vec{f^*}) = 0$ (i.e. the solution to our ODE). Now, during our iterations it is possible that we end up near a local minimum where $\nabla M(f_k) = 0$, but $M(\vec{f^*}) \neq 0$. This will cause our line search to give $\alpha_k = 0$, and cause $J(f_k)$ to become singular, which in turn causes our Newton step to become undefined.

To solve this problem, we use a modified Gauss-Newton (GN) step, defined as:

$$\vec{p_k} = -(J_k^T J_k + \lambda I)^{-1} J_k^T \vec{F}(f_k), \tag{4.14}$$

where λ_k is called the forcing term, which ensures that the step is always defined, even near non-zero roots of M. This also allows our line search to always give us a finite step length. Choosing the value for λ_k is not trivial. If the value is too high, then the step direction becomes closer to the steepest decent direction (since as $\lambda_k \to \infty$, $p_k \to -J_k^T \vec{F}(f_k)$), and fast convergence is lost. If the value for λ_k is too small, then near non-zero roots of M, the length of each step becomes very small, which requires the method to run for many iterations before converging. Through experimentation, we find that a fixed value of $\lambda_k = 0.001$ works well for finding steady-state vortex profiles with our chosen parameters [15].

To find steady-state radial profiles, we use Eqs. (4.10), (4.14), and (4.12) along with the backtracking line search. Our stopping criterion is when $M(\vec{f}) < \sqrt{\epsilon_{\text{mach}}}$, where ϵ_{mach} is the machine epsilon of our computational environment (in this case MATLAB, so $\sqrt{\epsilon_{\text{mach}}} \approx 1.49 \times 10^{-8}$). As an example run, we choose $\Omega = 0.25$ and $m = 2$ in Eq. (4.10) and, after 55 steps, we get the results shown in Fig. (4.3). We see that between iteration step 3 and 50, the GN does not make much progress. This is due to the presence of a nearby non-zero local minimum. To show that the GN solution is truly the radial profile of a steady-state vortex solution, we use it as an initial condition to our full two dimensional simulation in Sec. 7.2 and, as will be discussed there, we see that it indeed a steady-state solution.

Now we have the ability to find steady-state vortex solutions for any charge given a reasonable ansatz. However, as we have seen in Fig 4.3, there is a very noticeable difference between the shape of the VA1 profile and the GN converged solution. This is because the VA ansatz we have is not a good approximation to the true solution for charges greater than 1. In

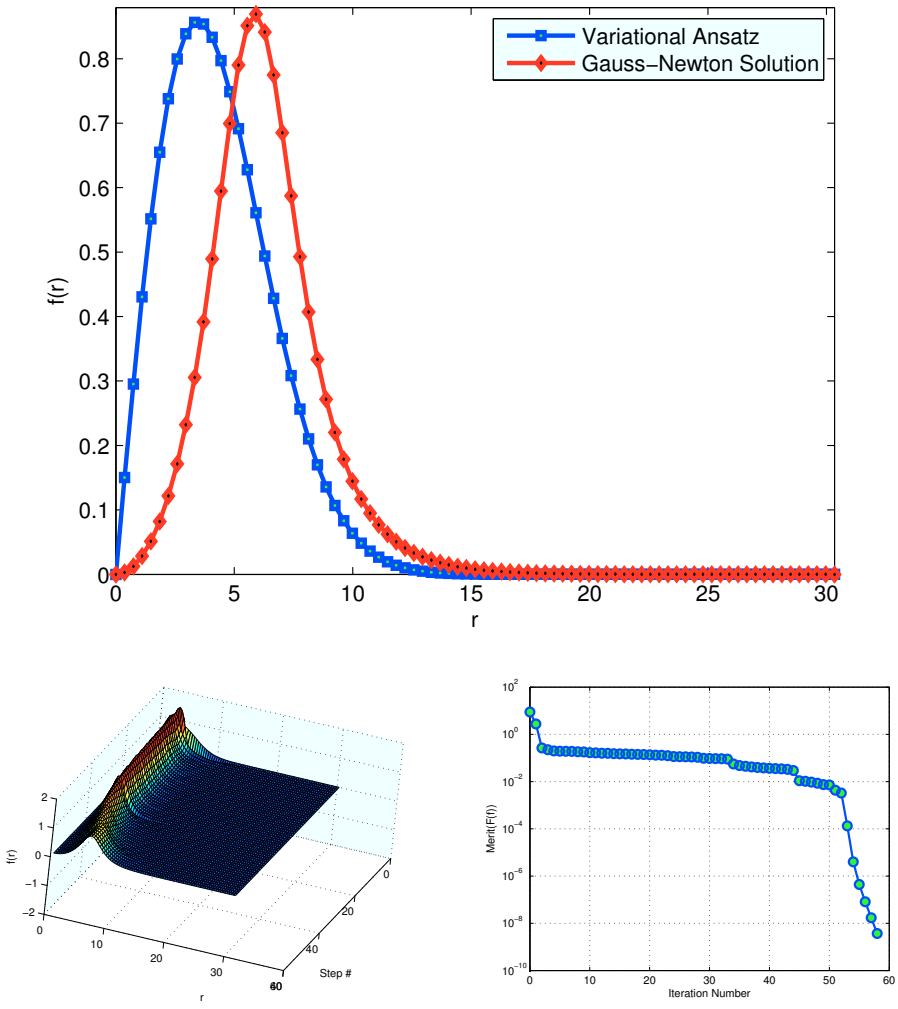

Figure 4.3. A typical example of running the GN routine to find a steady-state radial profile for a two-dimensional vortex solution to the NLS. For the run shown, we have set $\Omega = 0.25$ and $m = 2$. The initial profile is the variational ansatz VA1. The run takes 55 iterations to converge. Top: Plot of the VA1 profile (in blue) compared to the converged GN profile (in red). Bottom Left: Plots of the radial profile for each iteration of the GN routine starting with VA1 and ending with the GN converged solution. Bottom right: Plot of the sum-of-squares merit function, Eq. (4.12), per iteration step. It is noticeable that the steps make little progress between step 3 and 50, due to the presence of a non-zero local minimum.

fact, for very high charges, the VA is so bad, that the numerical optimization does not converge to a vortex profile, but rather to the zero trivial solution. Thus, we would like to have a better ansatz if possible, in order to test the theory for higher charges. If we look at Ref. [16], we see that having $r^{|m|}$ instead of r as the prefactor to the exponential in Eq. (4.7) could be expected to better capture the higher charge profiles. After exploring this option, we find that even though the updated VA ansatz can approximate higher charges better than the first one, it is a complicated expression difficult to work with, and also eventually breaks down as $|m|$ gets large. Therefore, we choose to explore another possible VA ansatz, a sech soliton profile.

4.3 Asymptotic Analytic Solution for High Charges

From numerical experiments using the GN routine, we observe that higher charge vortices (for the same Ω) have larger radii as shown in Fig. 4.4. We also notice (for example,

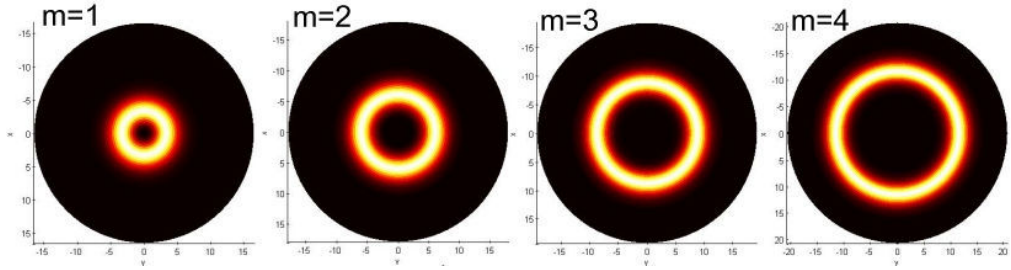

Figure 4.4. Plots of the modulus squared for vortices of charge $m = 1, ..., 4$ found using the GN routine. We see that for higher m (with the same Ω, chosen here to be $\Omega = 0.25$), the vortex has a larger radius.

in Fig. 4.3) that they have a profile that resembles the classic sech soliton solution to the one-dimensional NLS ($i\Psi_t + \Psi_{rr} + s\,|\Psi|^2\Psi = 0$):

$$\Psi(r,t) = \sqrt{\frac{2\,\Omega}{s}}\,\mathrm{sech}\left[\sqrt{\Omega}\,(r - r_c)\right] e^{-i\Omega t},$$

where r_c is the center position of the soliton. In order to find an approximate sech radial profile for a vortex, we once again use a VA as in Sec. 4.1, but utilize some asymptotically justified simplifications along the way. First, we notice that the Lagrangian of Eq. (4.4) can be written in terms of the constants of Eq. (2.11) as:

$$L = 2\pi[\Omega\,C_1 + m^2\,C_3 + C_2 - \frac{1}{2}\,C_4], \tag{4.15}$$

where we have now explicitly set $s = +1$. We use a one-dimensional soliton sech ansatz similar to that used in Ref. [17]:

$$f(r) = \sqrt{B}\,\mathrm{sech}\left(\sqrt{\frac{B}{2}}(r - r_c)\right). \tag{4.16}$$

Now assuming r_c to be large, we can approximate the C-constants as follows:

$$C_1 = \int_0^\infty B\,\mathrm{sech}^2\left(\sqrt{\frac{B}{2}}(r - r_c)\right) r\,dr = 2\ln\left(1 + e^{\sqrt{2B}r_c}\right) \tag{4.17}$$

$$\approx r_c\sqrt{8B}, \tag{4.18}$$

$$C_2 = \int_0^\infty \frac{B^2}{2}\,\mathrm{sech}^2\left(\sqrt{\frac{B}{2}}(r - r_c)\right)\,\tanh^2\left(\sqrt{\frac{B}{2}}(r - r_c)\right) r\,dr$$

$$= \frac{B}{3\left(1 + e^{\sqrt{2B}r_c}\right)^2}\left[\ln\left(1 + e^{\sqrt{2B}r_c}\right)\left(\left(e^{\sqrt{2B}r_c}\right)^2 + e^{\sqrt{2B}r_c} + 1\right) + 2\,e^{\sqrt{2B}r_c}\right]$$

$$\approx \frac{1}{3}r_c\sqrt{2B^3}. \tag{4.19}$$

The C_3 integral does not converge. However, since we assume r_c to be large, the r in the integrand can be viewed as a constant (which we choose to be the center of the sech, i.e. r_c) and so we have:

$$C_3 = \int_0^\infty \frac{1}{r^2}\,B\,\mathrm{sech}^2\left(\sqrt{\frac{B}{2}}(r - r_c)\right) r\,dr \tag{4.20}$$

$$\approx \frac{1}{r_c}\int_0^\infty B\,\mathrm{sech}^2\left(\sqrt{\frac{B}{2}}(r - r_c)\right)\,dr = \frac{\sqrt{8B}}{r_c}\,\frac{e^{\sqrt{2B}r_c}}{(1 + e^{\sqrt{2B}r_c})}$$

$$\approx \frac{\sqrt{8B}}{r_c}, \tag{4.21}$$

$$C_4 = \int_0^\infty B^2\,\mathrm{sech}^4\left(\sqrt{\frac{B}{2}}(r - r_c)\right) r\,dr = 4\,C_2 \tag{4.22}$$

$$\approx \frac{4\sqrt{2}}{3}r_c\,B^{3/2}. \tag{4.23}$$

Using these approximations, we get:

$$L = \frac{2\pi}{3}\sqrt{2B}\,r_c\left(6\,\Omega + 6\,\frac{m^2}{r_c^2} - B\right).$$

The Euler-Lagrange equations:

$$\frac{\partial L}{\partial B} = 0, \qquad \frac{\partial L}{\partial r_c} = 0,$$

lead us to the solution:

$$B = 3\Omega, \qquad r_c = \sqrt{\frac{2m^2}{\Omega}}, \tag{4.24}$$

and so our new ansatz (denoted as VA2) is:

$$f(r) = \sqrt{3\,\Omega}\,\mathrm{sech}\left[\sqrt{\frac{3\,\Omega}{2}}\left(r - \sqrt{\frac{2m^2}{\Omega}}\right)\right]. \tag{4.25}$$

This solution has a problem at $r = 0$, since by definition, we should have $f(0) = 0$ for any charge $|m| > 0$. However, it does capture the shape and position of the numerically 'exact' solution very well, and for higher m, its value at $r = 0$ is close to zero.

To see this, we find radial profiles using our GN routine for $m = 1, ..., 30$, and plot in Fig. 4.5 the sum-of-squares error between Eq. (4.25) and the numerically 'exact' solution for each profile, the number of steps needed for the GN routine to converge for each m, as well as the analytic and numerical profiles for $m = 1, ..., 8$. We see that our ansatz is an extremely good approximation to the numerically 'exact' solution, and therefore we can use it to predict K_{crit} and growth rates analytically. In fact, as seen in Fig. 4.5, when $m > 8$, the VA2 ansatz only takes one GN step to converge.

Now we are ready to pick test cases to make stability predictions of the azimuthal modes and check those predictions against numerical simulations. To do this, we have to choose parameters, specifically m and Ω. We shall now see that, without loss of generality, we only need to pick one value for Ω for all our test cases.

4.4 Solution Invariance

As we will see in Chap. 5, the K_{crit} derived from VA2 (as well as that from VA1) only depends on m, which implies that for any choice of Ω, we can expect the same K_{crit}, even though a different Ω produces a vortex profile of different height, width, and position. This is because every choice of Ω (for the same m) actually yields exactly the same solution, but with f and r rescaled. Thus, since it is the same solution, we would expect to find the same K_{crit}. This helps in testing the MI analysis from Chap. 3, because we only have to simulate one choice of Ω for any choice of m. To show this explicitly, we re-write Eq. (4.9) in its expanded form:

$$-m^2\frac{1}{r^2}f - \Omega f + \frac{1}{r}\frac{df}{dr} + \frac{d^2f}{dr^2} + sf^3 = 0. \tag{4.26}$$

We then make the following transformations:

$$\Omega = \beta\hat{\Omega}, \qquad f = \alpha F, \qquad r = \gamma R.$$

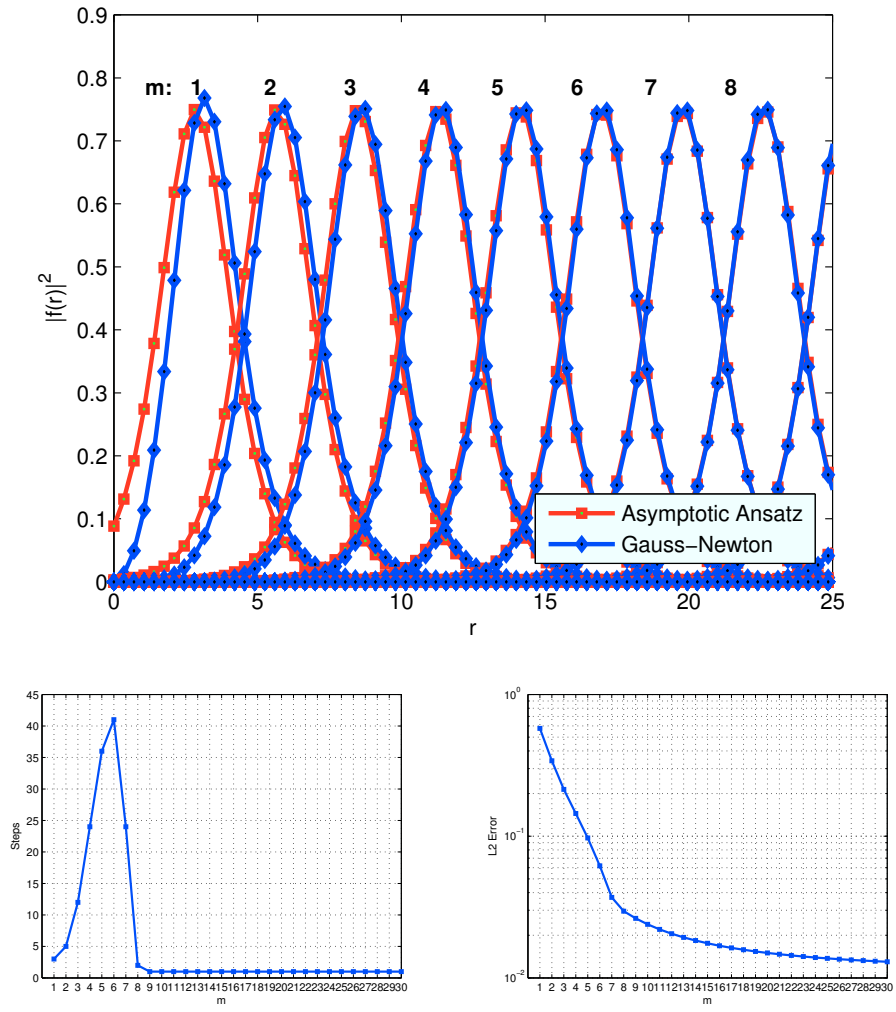

Figure 4.5. Comparison between VA2 and the numerically 'exact' GN solution for various charges. Top: Radial profiles of VA2 (red) and converged GN (blue) for vortex charges of $m = 1, ..., 8$. We notice that the VA2 captures the GN solution very well, and as m increases, the VA2 seems to converge to the GN profiles. Bottom left: Plot of the number of iterations needed in GN routine to converge the VA2 ansatz for $m = 1, ..., 20$. We see that at first, the GN routine takes more iterations as m increases, but after $m = 6$, the number of iterations decrease rapidly and after $m = 9$, the GN only requires one step before converging the VA2. Bottom right: Plot of the percent error between the sum of squares of the VA2 ansatz, and that of the GN converged profiles for $m = 1, ..., 20$. We see that at first, the error decreases exponentially as m increases, and then the error levels out.

Transforming Ω is essentially rescaling time. Inserting these rescalings into Eq. (4.26), and multiplying through by α/γ^2, we get:

$$-m^2\frac{1}{R^2}F - \frac{1}{\beta\gamma^2}\hat{\Omega}F + \frac{1}{R}\frac{dF}{dR} + \frac{d^2F}{dR^2} + \frac{1}{\alpha^2\gamma^2}sF^3 = 0.$$

If we require that:

$$\beta\gamma^2 = 1, \qquad \alpha^2\gamma^2 = 1,$$

namely:

$$\alpha = \sqrt{\beta}, \qquad \gamma = \frac{1}{\sqrt{\beta}} = \frac{1}{\alpha},$$

we obtain:

$$-m^2\frac{1}{R^2}F - \hat{\Omega}F + \frac{1}{R}\frac{dF}{dR} + \frac{d^2F}{dR^2} + sF^3 = 0,$$

which means we have the same dynamics as Eq. (4.26) after appropriate rescalings of space and the solution. Therefore, although different values of Ω will yield different growth rates for each mode (since it is a time rescaling), the K_{crit} will be the same. Therefore, without loss of generality, we only need to pick one Ω value for all the simulation runs of different charges.

Now that we have a handle on the parameters, we are ready to make our predictions.

CHAPTER 5

THEORETICAL PREDICTIONS

In this chapter, we formulate our predictions for the test cases that we will simulate. First, we derive analytic expressions for the predictions using the two variational anzätze, VA1 and VA2 defined in the previous chapter. Then, we use our Gauss-Newton routine to find the numerically 'exact' steady-state profiles, and use them to formulate predictions of the growth rates of perturbed azimuthal modes as well as the critical mode. Finally, we compare our numerical predictions with the analytical ones, and show that as m increases, the two sets converge.

5.1 ANALYTICAL PREDICTIONS

We begin by restating our expressions for the growth rates of each mode, and for the critical mode from Sec. 3.3:

$$\lambda = \frac{C_3}{C_1}\sqrt{K^2\,(K_{\text{crit}}^2 - K^2)}, \qquad K_{\text{crit}} = \pm\sqrt{2\frac{C_4}{C_3}}. \tag{5.1}$$

where we have explicitly set $s = +1$, and we are ignoring the negative eigenvalues. In addition, we can derive the maximum growth rate for any charge, as well as the mode which is closest to exhibiting that growth rate. To do this, we simply take the derivative of the growth rates with respect to K and set the result to zero. Then we solve for K, giving us the mode associated with the maximum growth rate:

$$K_{\text{max}} = \frac{1}{\sqrt{2}}\,K_{\text{crit}} = \pm\sqrt{\frac{C_4}{C_3}}. \tag{5.2}$$

Inserting this back into the growth rate equation, we find the maximum growth rate:

$$\lambda_{\text{max}} = \frac{C_4}{C_1}. \tag{5.3}$$

To formulate our analytic predictions, we need to find expressions for C_1, C_3, and C_4. For VA1, we can integrate these constants directly and we get:

$$\begin{aligned} C_1^{\text{va1}} &= 4\,(m+1), \\ C_3^{\text{va1}} &= 4\,\Omega, \\ C_4^{\text{va1}} &= 8\,\Omega\,(m+1), \end{aligned}$$

which lead to:

$$\begin{aligned} K_{\text{crit}}^{\text{va1}} &= 2\sqrt{m+1}, \\ \lambda^{\text{va1}} &= 2\,K\Omega\,\frac{\sqrt{m+K^2}}{m+1}, \\ K_{\text{max}}^{\text{va1}} &= \pm\sqrt{2(m+1)}, \\ \lambda_{\text{max}}^{\text{va1}} &= 2\,\Omega. \end{aligned} \tag{5.4}$$

For VA2, we already evaluated the C-constants (with asymptotic simplifications) during its derivation in terms of B and r_c in Eqs. (4.17), (4.20), and (4.22). Inserting Eq. (4.24) into those expressions yields:

$$\begin{aligned} C_1^{\text{va2}} &= 4\sqrt{3}\,m, \\ C_3^{\text{va2}} &= 2\sqrt{3}\,\frac{\Omega}{m}, \\ C_4^{\text{va2}} &= 8\sqrt{3}\,\Omega m, \end{aligned}$$

which lead to:

$$\begin{aligned} K_{\text{crit}}^{\text{va2}} &= \pm 2\sqrt{2}m, \\ \lambda^{\text{va2}} &= K\Omega\,\frac{\sqrt{8m^2-K^2}}{2m^2}, \\ K_{\text{max}}^{\text{va2}} &= \pm 2m, \\ \lambda_{\text{max}}^{\text{va2}} &= 2\,\Omega. \end{aligned} \tag{5.5}$$

We notice that if we set $m = 1$, then the predictions of K_{crit}, K_{max}, and λ_{max} for VA1 and VA2 are identical:

$$\begin{aligned} K_{\text{crit}}^{\text{va1}} &= K_{\text{crit}}^{\text{va2}} = \pm 2\sqrt{2}, \\ K_{\text{max}}^{\text{va1}} &= K_{\text{max}}^{\text{va2}} = \pm 2, \\ \lambda_{\text{max}}^{\text{va1}} &= \lambda_{\text{max}}^{\text{va2}} = 2\Omega. \end{aligned}$$

This is understandable since VA1 was a good approximation to an $m = 1$ vortex profile. Another observation is that for VA2, the mode where the maximum growth rate occurs is at an integer value of K, while the critical mode is never integer valued. We therefore would expect to always be able to see the maximum growth rate materialized in a randomly perturbed simulation. Also, we see that the maximum growth rate is independent of m, while the mode which exhibits that growth rate is independent of Ω (which is understandable since $K_{\text{max}} = 1/2\,K_{\text{crit}}$).

Using the results for VA2, and setting $\Omega = 0.25$, we plot the predicted growth rates of the unstable modes for charges $m = 1, ..., 5$ in Fig. 5.1. We observe that as we mentioned before, every charge exhibits the same maximum growth rate, and that it occurs at the mode $K = 2m$.

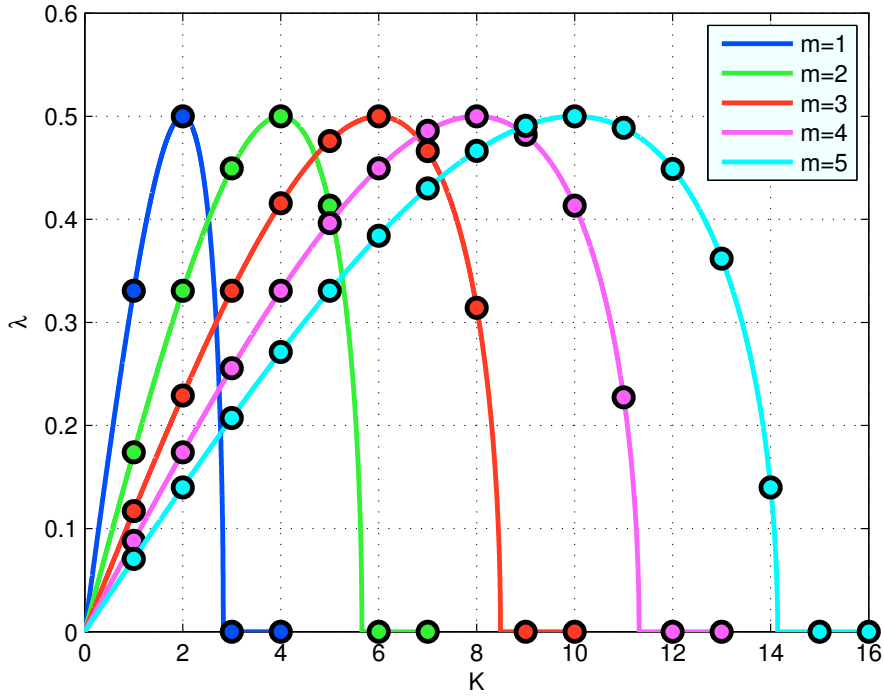

Figure 5.1. Analytical predictions of growth rates of perturbations of azimuthal modes (K) for vortices with $\Omega = 0.25$ and charges $m = 1, ..., 5$ using the VA2 ansatz predictions of Eq. (5.5). Each vortex displays the same maximum growth rate, which occurs at mode number $K = 2m$. We see that for each m, after the critical mode, the growth rate predictions for each K become 0 indicating that the perturbations after the critical mode are stable.

Now that we have analytical predictions for the growth rates of each mode and for the critical mode, we use our GN routine to formulate our numerical predictions.

5.2 Numerical Predictions

To make our numerical predictions for the growth rates of each mode, and the critical mode, we need to numerically integrate C_1, C_3, and C_4 using our numerically 'exact' radial profiles obtained by the use of the GN routine. The accuracy of the integrals needed will

depend on grid spacing, and their sensitivity around $r = 0$. We denote these predictions as λ^{num}, $K_{\text{crit}}^{\text{num}}$, $\lambda_{\text{max}}^{\text{num}}$, and $K_{\text{max}}^{\text{num}}$ analogous to the analytical predictions of Eqs. (5.4) and (5.5).

There is a way to check how good our numerical integration of the C-constants are. If we formulate the dispersion relationship of the unsimplified quasi-one-dimensional azimuthal PDE of Eq. (2.13), we get:

$$\Omega = -\frac{C_2}{C_1} - m^2 \frac{C_3}{C_1} + \frac{C_4}{C_1} \tag{5.6}$$

Since we choose Ω explicitly when we run our GN routine, we can test the combined error of the GN routine and how good our C-constant calculations are, by inserting them into Eq. (5.6) and checking if it indeed gives us back our original Ω. (We obviously need to numerically integrate C_2 as well to do this, in which case we compute the required expression for df/dr by using a central difference approximation - a further source of small numerical error.)

For $\Omega = 0.25$, and $m = 1$, we get $\Omega_{\text{num}} = 0.23408$, which is a sizable error (about 6 percent). However, we note that as we increase m, this error decreases exponentially, then increases to level out around $10^{-2.5}$ as is shown in Fig. 5.2.

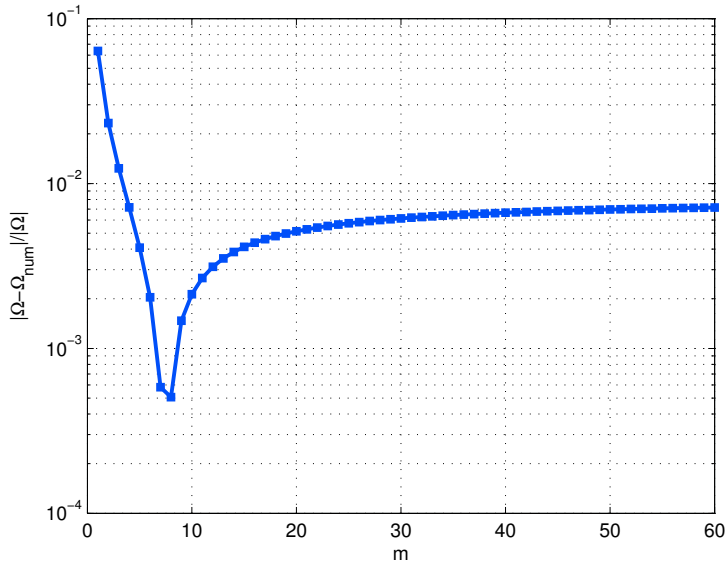

Figure 5.2. Relative error between the initial chosen value of Ω (here, we use $\Omega = 0.25$) to use in Eq. (4.10), versus the value numerically computed from Eq. (5.6) using the GN-converged radial profile for vortex charges $m = 1, ..., 60$. The error drops exponentially as m increases, and then 'bounces' to level off at a relative error of around $10^{-2.5}$. The grid spacing for each run is $\Delta r = 0.35$, and the maximum radius is set to the point where VA2 evaluates at $\sqrt{\epsilon_{\text{mach}}}$ for that specific charge (this maximum radius choice is discussed in more detail in Sec. 6.2).

Since the error in Ω emerges from the C-integrals, and the C-integrals are what we use to make our numerical growth rate and critical mode predictions, the error in Ω can be very relevant, especially for lower m. It is this error that we believe accounts for some of the discrepancies we will see in our growth rate comparisons in Sec. 7.2.

Keeping the error in our C-integrals in mind, we compute our numerical predictions for vortex charges $m = 1, ..., 5$, and plot the growth rates in Fig. 5.3.

We see that these numerical predictions are very close to the VA2 predictions in Fig. 5.1. We now compare the two sets of predictions in more detail and show that, as we expected, the two sets of predictions converge for high m.

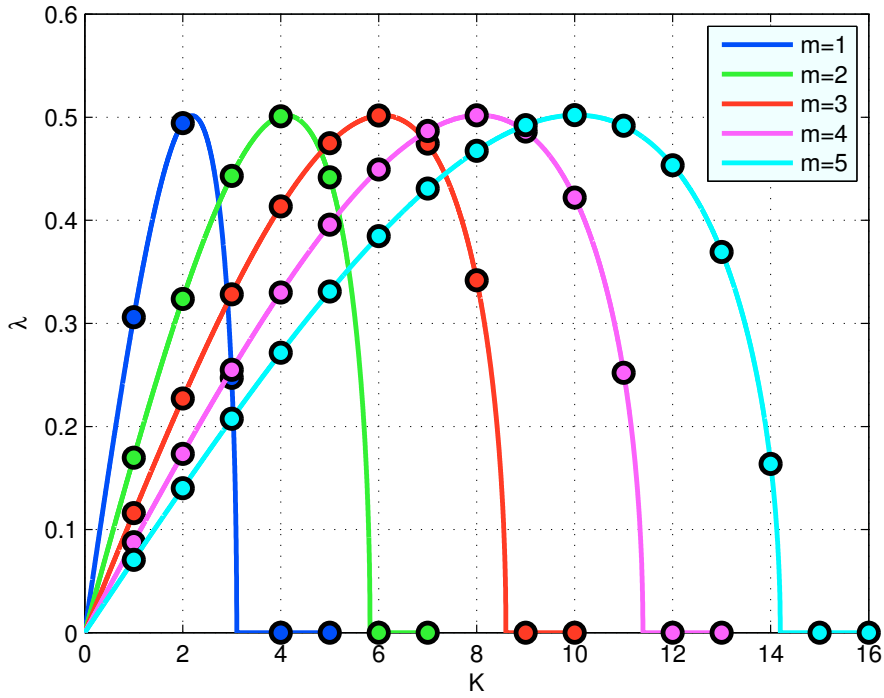

Figure 5.3. Numerical predictions of growth rates of perturbations of azimuthal modes (K) for vortices with $\Omega = 0.25$ and charges $m = 1, ..., 5$ using the GN routine to converge the VA2 ansatz into a numerically 'exact' solution. The predictions are made numerically integrating the constants of Eq. (5.1). Each vortex displays roughly the same maximum growth rate, which occurs at approximately mode number $K = 2m$. We see that for each m, after the critical mode, the growth rate predictions for each K become 0 indicating that the perturbations after the critical mode are stable.

5.3 Analytical and Numerical Comparisons

We have seen in Fig. 4.5 that the VA2 profile converges to the numerically exact radial profile for high m. Therefore, we can expect that the analytical stability predictions derived from VA2 and the numerical stability predictions computed from the GN solution should behave accordingly. To show this, we compute K_{crit} and λ_{max} both numerically and analytically for $m = 1, ..., 60$. As shown in Fig. 5.4, we see that the predictions for K_{crit} converge, but they level out at a relative error of about 10^{-3}, which is an acceptable level of error. This is because we are only concerned with integer values for K (since they are mode numbers), and therefore, unless K_{crit} is within 0.1% of an integer value, such a level of error will have no practical effect on our critical mode prediction.

Due to this convergence to an acceptable error, we can safely state that VA2 may be used to analytically predict stability of high charged vortices. We present our final numeric and analytic predictions for the growth rates for the azimuthal modes in Table 5.1 along with the percentage difference between them. We see once again, that our VA2 can be used to predict the MI almost as accurately as our numerical solution.

Now that we have our growth rate and critical mode predictions, as well as a handle on their errors, we are ready to simulate a vortex in the full two-dimensional system to put them to the test. To do this, we require a numerical method for integrating the two-dimensional NLS.

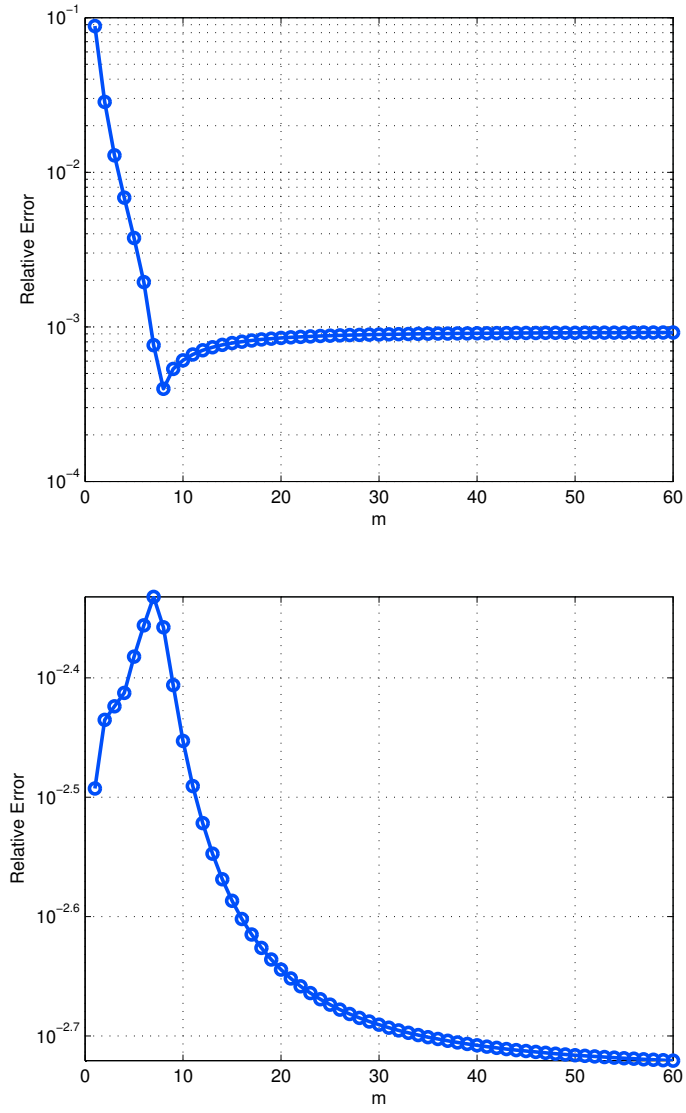

Figure 5.4. Relative error between numerical and analytical predictions of the critical mode K_{crit} (top) and the maximum growth rate λ_{max} (bottom). The analytical predictions are derived from the VA2 predictions of Eq. (5.5), while the numerical predictions are derived from Eqs. (5.1) and (5.3) by numerically integrating the GN-converged profiles. We notice that the error in the critical mode decreases exponentially as m is increased, then rises slightly before leveling off at around 10^{-3}. This 'bounce' effect in the error is similar to the one observed in Fig. 5.2. For the maximum growth rate, we see that the error actually increases, and then decreases quickly to level off around 10^{-3} as well.

Table 5.1. Numerical and Analytical Predictions of Growth Rates of Azimuthal Modes $K = 1, ..., 9$ of Vortices with Charges $m = 1, ..., 5$ with the Percent Difference between the Two Predictions. The two predictions are made as described in Fig. 5.4. We notice that the errors between the growth rate predictions become very small as m is increased.

$m \rightarrow$	1			2			3		
K	NUM	VA2	%	NUM	VA2	%	NUM	VA2	%
1	0.306	0.331	8.04	0.170	0.174	2.46	0.116	0.117	0.90
2	0.494	0.500	1.13	0.324	0.331	2.15	0.227	0.229	0.85
3	0.247	0	100	0.443	0.450	1.45	0.328	0.331	0.74
4	0	0	0	0.501	0.500	0.21	0.413	0.416	0.56
5	0	0	0	0.442	0.413	6.41	0.475	0.476	0.24
6	0	0	0	0	0	0	0.502	0.500	0.34
7	0	0	0	0	0	0	0.474	0.466	1.72
8	0	0	0	0	0	0	0.342	0.314	8.05
9	0	0	0	0	0	0	0	0	0

$m \rightarrow$	4			5		
K	NUM	VA2	%	NUM	VA2	%
1	0.088	0.088	0.29	0.071	0.071	0.04
2	0.174	0.174	0.28	0.140	0.140	0.05
3	0.255	0.256	0.25	0.207	0.207	0.06
4	0.330	0.331	0.20	0.271	0.271	0.07
5	0.396	0.396	0.13	0.331	0.331	0.09
6	0.449	0.450	0.03	0.385	0.384	0.12
7	0.487	0.486	0.12	0.431	0.430	0.16
8	0.502	0.500	0.38	0.467	0.466	0.22
9	0.486	0.482	0.86	0.492	0.491	0.29

CHAPTER 6

NUMERICAL METHOD

In this chapter, we describe the numerical methods utilized to simulate the two-dimensional NLS, and the technique used to record the growth rate of the azimuthal modes, in order to test our MI predictions.

6.1 FINITE DIFFERENCE ON A POLAR GRID

As was mentioned in Sec. 2.1, the natural coordinate system for studying MI of vortices is polar. Therefore, we discretize our two-dimensional plane as shown in Fig. 6.1. The radial direction is discretized in the same manner as was shown in Fig. 4.1. The

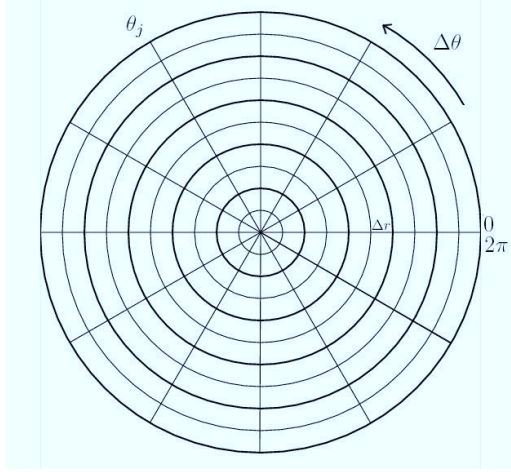

Figure 6.1. Example of a discretized polar coordinate grid. The radial direction is discretized as described in Fig 4.1. The azimuthal direction has grid spacing of $\Delta\theta$, so that $\theta_j = j\Delta\theta$, $j = 1, ..., J$ for $\theta \in [0, 2\pi]$. The disk shown here (which is much coarser than the grid we will use in the simulations) has a radial resolution of $n = 10$ and an azimuthal resolution of $J = 12$.

azimuthal direction is discretized in a similar manner, with grid spacing of $\Delta\theta$, so that $\theta_j = j\Delta\theta$, $j = 1, ..., J$ for $\theta \in [0, 2\pi]$. We also must discretize time, in which case Δt is the time step, so that $t_n = n\Delta t$. Using this discretization, we have that:

$$\Psi(r, \theta, t) = \Psi(r_i, \theta_j, t_n) \equiv \Psi^n_{i,j}.$$

To integrate the NLS, we treat the time derivative separately from the spatial derivatives. Therefore we write Eq. (2.5) as:

$$\Psi_t = F(\Psi) = i(\nabla^2\Psi + s|\Psi|^2\Psi),$$

so that our time derivative scheme can simply evaluate F, which inside contains our spatial scheme, and the two are independent. For the time derivatives, we use the fourth order Runga-Kutta method as explained in Ref. [18]. This method calculates Ψ_t at different times within Δt, and then computes a weighted average to give Ψ^{n+1} to within $\mathcal{O}(\Delta t^5)$ accuracy (not counting the errors in the spatial scheme). The Runga-Kutta scheme is defined as:

$$\Psi^{n+1} = \Psi^n + \frac{\Delta t}{6}(k_1 + 2k_2 + 2k_3 + k_4), \tag{6.1}$$

$$k_1 = F(\Psi^n), \qquad k_2 = F(\Psi^n + \frac{\Delta t}{2}k_1),$$

$$k_3 = F(\Psi^n + \frac{\Delta t}{2}k_2), \qquad k_4 = F(\Psi^n + \Delta t k_3),$$

where $\Psi^n = \Psi^n_{i,j} \forall i, j$. We evaluate F at time n as:

$$F(\Psi_{i,j}) = i(\nabla^2\Psi_{i,j} + s|\Psi_{i,j}|^2\Psi_{i,j}), \tag{6.2}$$

where $\Psi_{i,j} = \Psi^n_{i,j}$. For evaluating the Laplacian in Eq. (6.2), we use the second order central difference scheme of Ref. [19]:

$$\nabla^2\Psi_{i,j} = \frac{1}{r_i}\frac{1}{\Delta r}\left(r_{i+\frac{1}{2}}\frac{\Psi_{i+1,j} - \Psi_{i,j}}{\Delta r} - r_{i-\frac{1}{2}}\frac{\Psi_{i,j} - \Psi_{i-1,j}}{\Delta r}\right) + \frac{1}{r_i^2}\frac{\Psi_{i,j+1} - 2\Psi_{i,j} + \Psi_{i,j-1}}{\Delta\theta^2}.$$

In order to speed up the computation time, we can limit the number of operations per time step by writing the Laplacian as:

$$\nabla^2\Psi_{i,j} = A_i(\Psi_{i+1,j} - \Psi_{i,j}) + B_i(\Psi_{i,j} - \Psi_{i-1,j}) + C_i(\Psi_{i,j+1} - 2\Psi_{i,j} + \Psi_{i,j-1}),$$

where the following are only computed once:

$$A_i = \frac{1}{\Delta r^2}\frac{r_{i+1/2}}{r_i}, \qquad B_i = -\frac{1}{\Delta r^2}\frac{r_{i-1/2}}{r_i}, \qquad C_i = \frac{1}{\Delta\theta^2}\frac{1}{r_i^2}.$$

The finite difference scheme as described is incomplete because we need to describe the boundary conditions. These can be more difficult to implement on a Polar grid than a Cartesian grid, but due to the specific properties of vortices, some of the difficulties can be circumvented.

6.2 BOUNDARY CONDITIONS

For a two-dimensional Polar grid, there are three boundary conditions that need to be addressed in using a finite difference scheme: (1) The $\theta = 0, 2\pi$ line, i.e. the periodicity of the θ direction, (2) The perimeter of the disk at $r = r_{\max}$, and (3) The center point at $r = 0$.

1. The $\theta = 0, 2\pi$ line is the simplest boundary condition to handle. All that is necessary is to slightly alter the θ-derivative in the Laplacian in order for it to be periodic at $\theta = 0, 2\pi$:

$$\begin{aligned} j = 0, J \qquad &\rightarrow \qquad \frac{\Psi_{i,1} - 2\Psi_{i,0} + \Psi_{i,J-1}}{\Delta\theta^2}, \\ j = J-1 \qquad &\rightarrow \qquad \frac{\Psi_{i,0} - 2\Psi_{i,J-1} + \Psi_{i,J-2}}{\Delta\theta^2}. \end{aligned} \tag{6.3}$$

2. The $r_{\max}$ boundary is a little more difficult. Ideally, one would want a 'transparent' boundary condition, but this can be difficult to implement. For our problem, we can get around this difficulty because we notice that if we set $r_{\max}$ to be sufficiently large, then the tail end of the vortex profile is very close to zero at the boundary. Thus we can simply have a Dirichlet condition of $\Psi(\theta, r_{\max}, t) = 0$. However, we must be careful in our choice of $r_{\max}$ because if we set the boundary to be identically zero too close to the vortex, we could be artificially damping any MI, thus causing a discrepancy in the growth rates. Also, the steady-state solution we get from the GN routine would not be the one we are looking for, but rather the solution of a 'walled-in' vortex.

Luckily, we have the extremely good approximate profile of Eq. (4.25) at our disposal. With this, we simply set our $r_{\max}$ to be large enough so that the value of Eq. (4.25) at $r = r_{\max}$ is small enough that we do not expect too much error arising from the boundary condition. For our problem, we use $\sqrt{\epsilon_{\text{mach}}}$ as our 'small enough' value, since we have previously used it as a zero value in our stopping criterion of the merit function in the GM routine. So, using Eq. (4.25) and setting it equal to $\sqrt{\epsilon_{\text{mach}}}$, yields:

$$r_{\max} = \sqrt{\frac{2}{3\Omega}}\,\text{arcsech}\left(\sqrt{\frac{\epsilon_{\text{mach}}}{3\Omega}}\right) + \sqrt{\frac{2m^2}{\Omega}}. \tag{6.4}$$

3. At $r = 0$, the finite difference scheme needs to evaluate $1/r_i$ terms, causing the center point to become a singularity. For our problem, there is an easy way to circumvent the singularity. Since all vortex solutions will, by definition, have $\Psi(0, \theta, t) = 0$, we can have a simple Dirichlet condition of zero at the center of the disk.

However, if we want to generalize our code to be able to simulate other initial conditions which are not identically zero at $r = 0$, we need to have a way to compute the NLS at the center point. To do this, we derive a second order approximation for the center point using the technique described in Ref [19]. We integrate Eq. (2.5) about the center point over a

disk of radius $\Delta r/2$:

$$\int\int_D \Psi_t r\, dr d\theta = \int\int_D i(\nabla^2\Psi + s|\Psi|^2\Psi) r\, dr d\theta.$$

The θ-derivative in the Laplacian becomes zero, since the center point is independent of θ. This, combined with performing the r-integral on the radial part of the Laplacian yields:

$$\int_0^{2\pi}\int_0^{\Delta r/2} \Psi_t r\, dr d\theta = i\left[\int_0^{2\pi} \frac{\partial\Psi}{\partial r}\frac{\Delta r}{2} d\theta + \int_0^{2\pi}\int_0^{\Delta r/2} s|\Psi|^2\Psi r\, dr d\theta\right].$$

We now discretize the spatial part of the equation, using a forward difference approximation to the r-derivative and approximating the integral that contains it over θ by a summation. The other integrals can now be approximated as the area of D times the integrands, and we get:

$$\Psi_t\left(\frac{\Delta r}{2}\right)^2\pi = i\left[\sum_{j=1}^{J}\frac{\Psi_{1,j}-\Psi_0}{\Delta r}\frac{\Delta r}{2}\Delta\theta + s|\Psi_0|^2\Psi_0\left(\frac{\Delta r}{2}\right)^2\pi\right],$$

where the value of Ψ at the center point is independent of θ, and is thus denoted Ψ_0. Rearranging the terms, and noting that $\Delta\theta = 2\pi/J$ gives the $F(\Psi_0)$ which we can now add to our finite difference scheme as a special case of Eq. (6.2):

$$\Psi_t = i\left(\frac{2}{\Delta r}\right)^2\left[\frac{1}{J}\sum_{j=1}^{J}\Psi_{1,j} - \Psi_0 + \left(\frac{\Delta r}{2}\right)^2 s|\Psi_0|^2\Psi_0\right]. \tag{6.5}$$

Now that we have our numerical scheme complete, we need to formulate initial conditions for the simulations. Specifically, we want to determine how to perturb each individual azimuthal mode of our steady-state vortex in order to study its MI.

6.3 Initial Conditions

In order to capture the growth rates of the individual modes, we want to have an initial condition which perturbs only a single mode. The general form for our initial condition is:

$$\Psi(r,\theta,0) = f(r)\left[1 + u(\theta,0) + iv(\theta,0)\right]e^{im\theta}, \tag{6.6}$$

where u and v are as defined in Sec. 3.2. If we want to perturb a single mode, K, we must also include the $-K$ term in the summations of Eq. (3.8) because it essentially is the same mode, with the same stability properties. Thus, for a single mode we have:

$$u(\theta,0) = \frac{1}{2\pi}\left[\hat{u}(K,0)e^{-iK\theta} + \hat{u}(-K,0)e^{iK\theta}\right],$$

$$v(\theta,0) = \frac{1}{2\pi}\left[\hat{v}(K,0)e^{-iK\theta} + \hat{v}(-K,0)e^{iK\theta}\right].$$

We need expressions for $\hat{u}$ and $\hat{v}$. Although we could simply set them to be equal to some small amplitude, ϵ, where $\epsilon \ll 1$, we want to make sure that our perturbation is in the direction of the eigenvectors of the growth rates of the mode being perturbed. As we saw in the phase plane of the left panel of Fig. 3.1, if we start with an arbitrary initial perturbation amplitude, it can take some time before we observe the growth rate we are trying to capture (this effect will be shown numerically in Sec. 7.1). Therefore, we formulate general solutions to $\hat{u}(K,0)$ and $\hat{v}(K,0)$ using the eigenvalues and eigenvectors of Eqs. (3.13) and (3.14). The general solutions at time 0 are:

$$\begin{aligned} \hat{u}(K,0) &= c_1 \frac{K}{K_{\text{crit}}} + c_2 \frac{-K}{K_{\text{crit}}}, \\ \hat{v}(K,0) &= c_3 \sqrt{1 - \left(\frac{K}{K_{\text{crit}}}\right)^2} + c_4 \sqrt{1 - \left(\frac{-K}{K_{\text{crit}}}\right)^2}, \end{aligned} \tag{6.7}$$

where c_1, c_2, c_3, and c_4 are arbitrary constants. The expressions for $\hat{u}(-K,0)$ and $\hat{v}(-K,0)$ are the same with the sign of K switched. We want to choose our constants so that both $\hat{u}$ and $\hat{v}$ are in the direction of the unstable eigenvector, and we can choose them so that $\hat{u}(K,0) = \hat{u}(-K,0)$ and $\hat{v}(K,0) = \hat{v}(-K,0)$. Choosing the constants carefully, and adding an ϵ term to make our perturbations small, we insert $\hat{u}$ and $\hat{v}$ into Eq. (6.7), and now have the resulting initial perturbation:

$$\begin{aligned} u(\theta,0) &= \frac{\epsilon}{2} \frac{K}{K_{\text{crit}}} (e^{-iK\theta} + e^{iK\theta}) = \epsilon \frac{K}{K_{\text{crit}}} \cos(K\theta), \\ v(\theta,0) &= \frac{\epsilon}{2} \sqrt{1 - \left(\frac{K}{K_{\text{crit}}}\right)^2} (e^{-iK\theta} + e^{iK\theta}) = \epsilon \sqrt{1 - \left(\frac{K}{K_{\text{crit}}}\right)^2} \cos(K\theta), \end{aligned}$$

where as before, $\epsilon \ll 1$. Inserting this into Eq. (6.6) yields the full initial condition:

$$\Psi(r,\theta,0;|K|) \equiv \Psi_{0;|K|} = f(r) \left[1 + \epsilon \left(\frac{K}{K_{\text{crit}}} + i \sqrt{1 - \left(\frac{K}{K_{\text{crit}}}\right)^2} \right) \cos(K\theta) \right] e^{im\theta}. \tag{6.8}$$

If we want to perturb multiple modes, we simply form a sum of Eq. (6.8):

$$\Psi(r,\theta,0) = \sum_{K=K_0}^{K_n} \Psi_{0;|K|}.$$

Now we have a way to perturb each mode in our simulation in order to record the growth rates of the perturbations to test our theory. We now describe how we record such growth rates during our simulations.

6.4 GROWTH RATE COMPUTATION

In this section, we describe how we measure the growth and compute the growth rates of the perturbed modes during our simulations of the NLS for comparison to the theoretical predictions.

We would like to directly record how the amplitudes of the real and imaginary parts of the azimuthally symmetric perturbation of Ψ grow over time. However, it is very difficult to record this growth due to the complex phase of the vortex. Therefore, we instead record the growth of the amplitudes of the MI from $|\Psi|$ which is expected to give the same growth rates.

To measure the amplitude of a modulational perturbation of $|\Psi|$, we extract the azimuthal crest at the center radius of the vortex. To do this, we find the maximum value of $|\Psi|$ along a radial cut of our disk for every θ, and temporarily store the values in a vector denoted as $\vec{\Psi}_{\text{crest}}$ as depicted in Fig. 6.2. We could save some computation time by assuming that the radial position of the maximum at one θ value will be the maximum for all θ, and thus simply extract $\vec{\Psi}_{\text{crest}}$ from the row corresponding to that radial position in our Ψ matrix. However, we do not do this because it is possible that there could be 'wiggling' instabilities in the radial directions, which would cause discrepancies in our MI measurements.

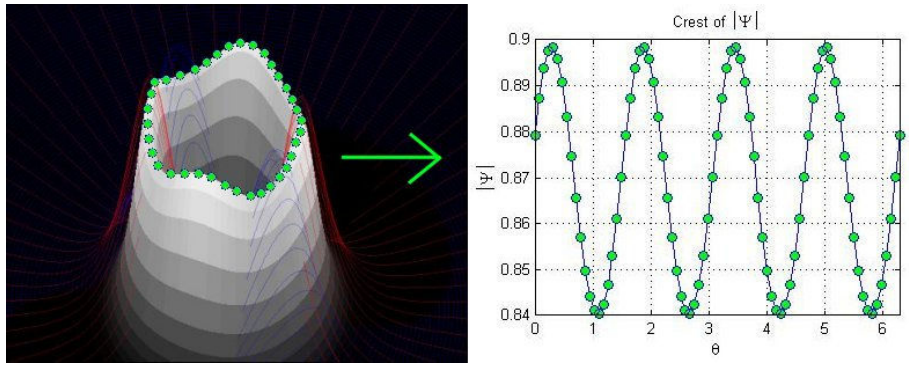

Figure 6.2. Illustration of central radius crest extraction. The maximum modulus value is found along the radial direction for each azimuthal angle (left) and is then stored in a one-dimensional array and plotted (right).

Once we have $\vec{\Psi}_{\text{crest}}$, we measure the growth of the perturbation mode by simply recording the amplitude and storing the result:

$$G(n) = |\max(\vec{\Psi}^n_{crest}) - \min(\vec{\Psi}^n_{crest})|,$$

where $G(n)$ is the amplitude of the perturbation at time $t = n\Delta t$. After the simulation is done, we plot $G(t)$ on a logarithmic scale and compare the result with the numerical prediction as shown in Fig. 6.3.

We then calculate the growth rate:

$$G_{\text{rate}}(t) = \frac{d(\ln G(t))}{dt},$$

by computing a central difference approximation for the derivative. We then plot $G_{\text{rate}}(t)$ along with the predicted growth rate as seen for a typical example in Fig. 6.4.

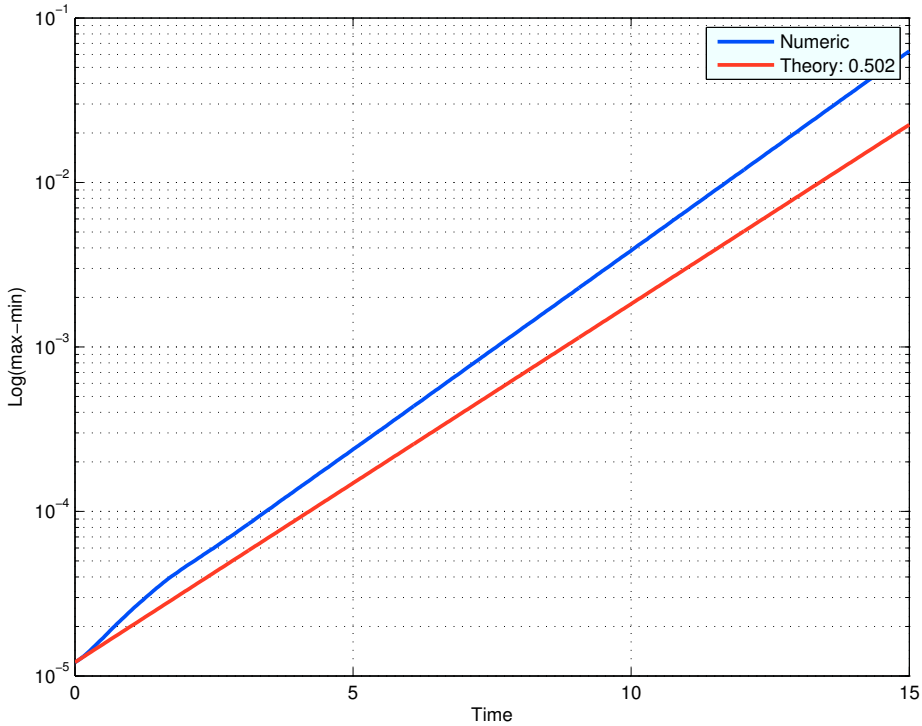

Figure 6.3. A typical example of plotting the growth over time of a single perturbed mode (here, $K = 6$) of a vortex (here, of charge $m = 3$) on a logarithmic scale. The blue line represents the time evolution of the amplitude of the modulus of the perturbed mode, while the red line is formed from an exponential function with the predicted growth rate starting with the same initial perturbation. For the simulation depicted here $\Omega = 0.25$ and all numerical parameters are set as in Eqs. (7.1) and (7.2).

We observe a large bump in growth rate at the start of the run in all our simulations, which shows that we have perturbed not in the direction of the two-dimensional eigenvector. This is because, as mentioned in Sec.2.2, our assumption that the vortex solution is separable is not true, but rather a very good approximation. Thus, the direction of the azimuthal eigenvectors will not be exactly that of the full two-dimensional eigenvectors, just close to

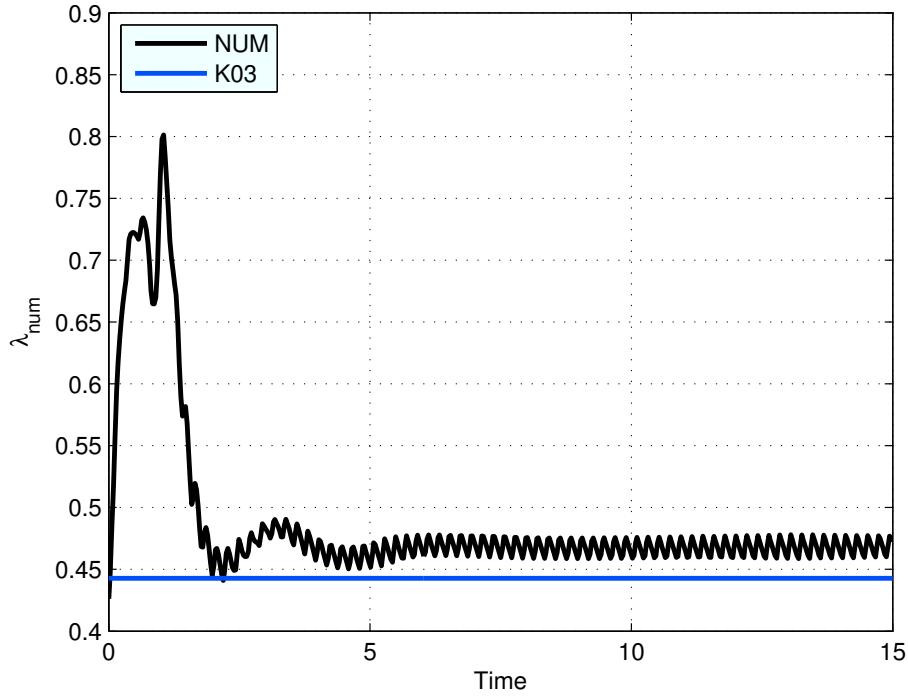

Figure 6.4. A typical example of plotting the growth rate over time of a single perturbed mode (here, $K = 3$) of a vortex (here, of charge $m = 2$). The growth rates are computed using a finite difference approximation of the logarithmic growth plot of the mode as shown in Fig. 6.3. The black line represents the time evolution of the growth rate of the perturbed mode, while the blue line represents the numerically predicted growth rate. We see that the perturbation takes around 5 time units to settle in the direction of the eigenvector. Also, in this example, we see that the growth rate computed from the simulation is slightly larger than that predicted. For the simulation depicted here $\Omega = 0.25$ and all numerical parameters are set as in Eqs. (7.1) and (7.2).

them, requiring some time for the perturbation to settle to the true eigenvectors. Because of this, we need to use a subset of the simulation run time for computing an average growth rate to compare to the predictions. This time span should start late enough in the run so that the system has settled onto the eigenvector, but end before the perturbation becomes so large that nonlinear effects become dominant. Selecting this time span after each run, we compute the average growth rate:

$$G_{\text{ave}} = \frac{1}{|t_e - t_s|} \sum_{t=t_s}^{t_e} G_{\text{rate}}(t) \Delta t,$$

where t_s is the beginning time index of our span, and t_e is the ending time. In Sec. 7.2, we use the computed G_{ave} for each K and m to compare with our theoretical predictions.

Now, along with our numerical scheme, we have a way to measure the growth rates of the perturbed modes. We are now ready to run our simulations to obtain our results.

CHAPTER 7

NUMERICAL RESULTS

In this chapter we present our MI results from integrating the NLS. We validate our numerical scheme by integrating the quasi-one-dimensional azimuthal equation of Eq. (3.3) and comparing the growth rates observed with those predicted by theory. We also show what effects perturbing in the direction of, or away from the eigenvectors have on the simulations. Finally, we simulate vortex solutions of the full two-dimensional NLS and record the growth rates of the perturbed azimuthal modes, and compare them to the theoretical predictions. The results are then analyzed and possible sources of error are discussed.

7.1 INTEGRATION OF THE AZIMUTHAL EQUATION

In this section we show the results of simulating the quasi-one-dimensional NLS of Eq. (3.3). We do this for two reasons. First, we can use the results to verify that our perturbation and stability analysis as well as our numerical method from Chap. 6 is valid, and that our perturbation growth is safely in the linear regime. Second, as noted in Sec. 6.3, we used the eigenvectors found in Sec. 3.3 in formulating our initial conditions for the perturbation of the azimuthal modes. By integrating Eq. (3.3), we can see what effect having a perturbation sightly off the eigenvector will have on the growth rate computation. This is important to know because since, as we have seen in Sec. 6.4, the two-dimensional vortex solutions are not completely separable.

For the simulation, the C_3 and C_4 terms are taken from the $m = 2$ GN profile integrals. The scheme used is the same Runga-Kutta and central differencing from Chap. 6, but altered to be one-dimensional with no radial part. All of the numerical parameters such as time step size, perturbation size, etc. are the same as will be shown in Sec. 7.2.

We start with an initial perturbation that is not aligned with the azimuthal eigenvectors:

$$\Psi_0 = (1 + \epsilon\cos(K\theta) + i\epsilon\sin(K\theta))e^{im\theta},$$

where K is the mode number, m is the vortex charge, and ϵ is the initial amplitude of the perturbation, which is set to $\epsilon = 0.00001$. The results for perturbing $K = 3$ and $K = \lfloor K_{\text{crit}} \rfloor$ (where $\lfloor x \rfloor$ denotes the floor function - i.e. the lowest integer less than x) are shown in Fig. 7.1.

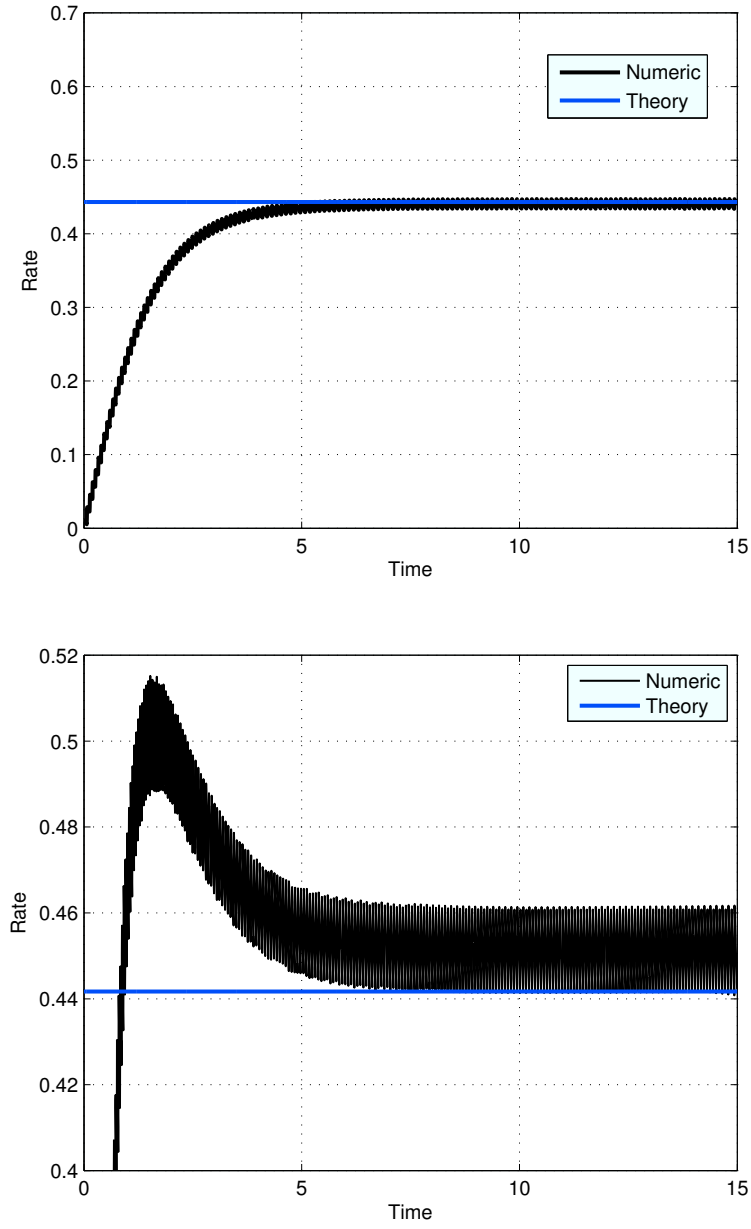

Figure 7.1. Examples of growth rate computations using an initial condition not in the direction of the azimuthal eigenvectors. The description and parameters used in making the plots are the same as those described in Fig. 6.4, but here with $K = 3$ (top) and $K = 5$ (bottom). We see that it takes about 5 time units for the perturbation to settle in the direction of the eigenvector. Also, for $K = 5$, we notice that the stabilized growth rate is larger than predicted.

The oscillations in the $K = \lfloor K_{\text{crit}} \rfloor$ case are due to discretization 'roll over', where since the perturbation is rotating in the azimuthal direction, the grid points corresponding to the top or bottom of the perturbation are moved, and for fewer grid points per mode, this causes oscillations in the growth rate, but leave the overall average growth rate unchanged.

We see in each case that it takes about 5 time units for the growth rates to settle. For $K = \lfloor K_{\text{crit}} \rfloor$, the stabilized growth rate is larger than predicted. If we perturb the system using the eigenvectors as in Eq. (6.8), then for the same two modes, we get the results in Fig. 7.2 (p. 48). We see that starting on the eigenvector is very beneficial, in that the growth rate settles almost immediately. However, for $K = \lfloor K_{\text{crit}} \rfloor$ we still get the larger than predicted growth rate. This is due to the fact we are near the bifurcation point, and thus the system is very sensitive. This is evident in the fact that for other vortex charges where $K = 5$ is unstable, but not near K_{crit}, we observe the growth rate much closer to that predicted (even with the same resolution). Therefore we may need to simulate modes near K_{crit} using a higher resolution.

To test this, we set the resolution very high ($J = 500$), and we get the result in Fig. 7.3 (p. 49). The result shown is much closer to the predicted growth rate than that depicted in Fig. 7.2. However, using a resolution of 500 for the θ direction in the full two-dimensional system is computationally undesirable, requiring very large computation times (since to keep the scheme stable for higher resolutions, we need to greatly decrease the time step). For the results in Sec.7.2 we will be using a more modest resolution of 80 for the θ direction and therefore may expect to see some small discrepancy between the theoretical predictions and the computed growth rate for modes close to K_{crit}.

Now that our numerical scheme is validated, as is our method for calculating the growth rates of the azimuthal modes, we move on to perform the simulations for the full two dimensional NLS.

7.2 Integration of Full Two-Dimensional System

Here we show our grow rate computation results of simulating vortex solutions of the full two-dimensional NLS. For all our simulations we set (without loss of generality) $\Omega = 0.25$, and the following numerical parameters:

$$\Delta r = 0.35, \qquad \Delta\theta = \frac{2\pi}{80}, \qquad \Delta t = 0.0005. \tag{7.1}$$

We use $J = 80$ for the azimuthal resolution so that we have at least around 10 grid points per wave period in our perturbed mode.

We first test our GN solution to make sure it is indeed a steady-state solution, keeping in mind that because of the finite-precision computational environment of the simulation, small random perturbations of size ϵ_{mach} are present which causes numerically-induced MI. To

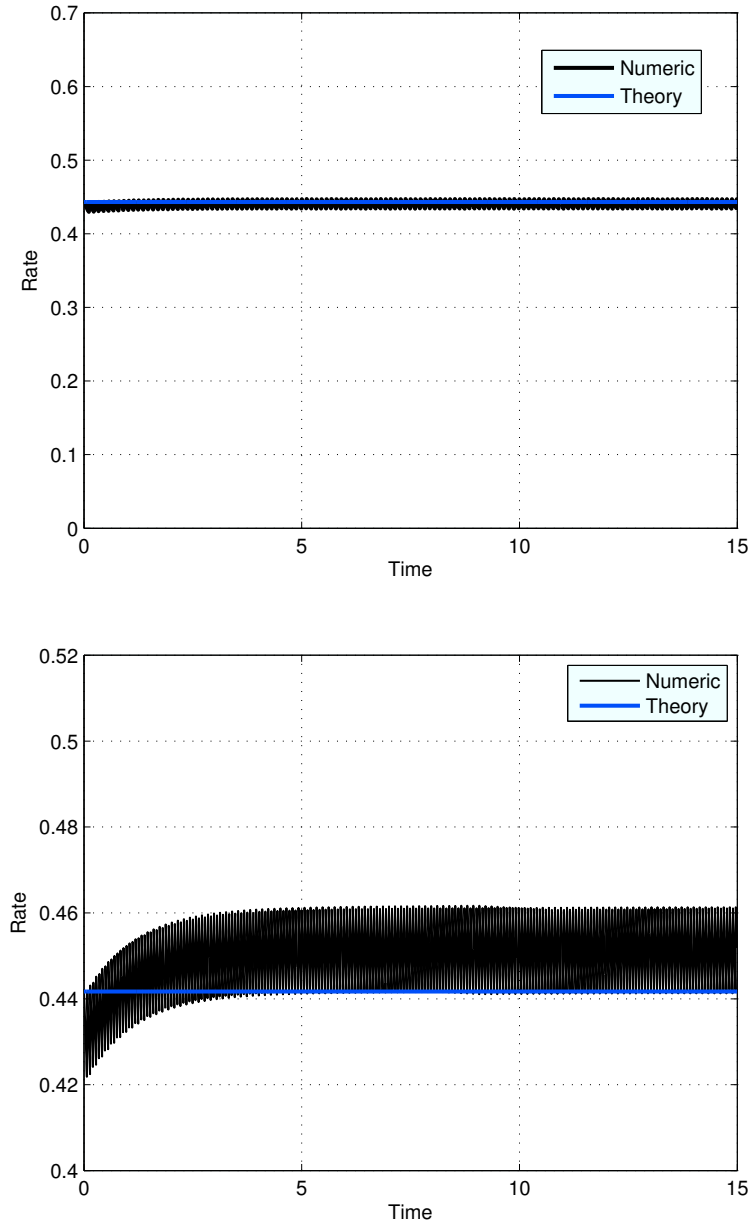

Figure 7.2. Examples of growth rate computations using an initial condition in the direction of the azimuthal eigenvectors. The description of the plots are as described in Fig. 7.1, and plotted on the same scale for easy comparison. We see that perturbing along the eigenvectors is helpful in that it now takes less time for the perturbations to exhibit a steady growth rate. However, for $K = 5$, we notice that the stabilized growth rate is still larger than predicted.

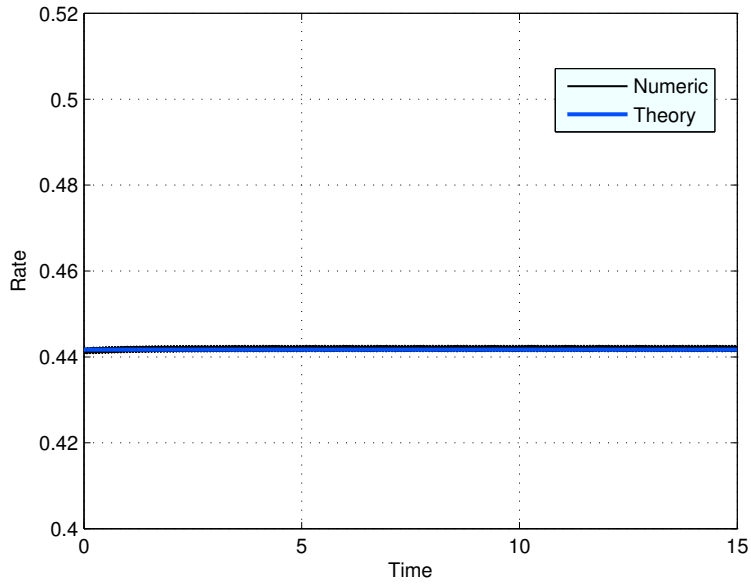

Figure 7.3. Growth rate computation for a higher resolution ($J = 500$) simulation corresponding to the case depicted in the bottom panel of Fig. 7.2. The plot is shown at the same scale for easy comparison. We notice that the simulated growth now exhibits the predicted growth rate, and that the 'roll-over' discretization effect has become barely noticeable. Therefore, we see that in order to properly capture the growth rate of azimuthal modes near K_{crit}, one needs to use a very large resolution.

test if the solution is steady, we run a simulation on the unperturbed vortex and record how the C-constants change over time. Specifically, we would like to know how K_{crit} and C_3/C_1 (which is the prefactor in the growth rate equation) change. This is important because if they change too much over the simulation, then our predictions (which are computed from the initial steady state condition) will be inaccurate over the time span of the simulation. If the constants change only very slightly before the numerically-induced MI takes effect, then we can consider our solution to be steady-state, and our predictions reliable.

For our vortex solutions (which as we saw in Sec. 5.2 all have very similar maximum growth rates) we find, after running unperturbed simulations, that the numerically-induced MI does not become large until after around 50 time units and, until then, the constants indeed change only slightly. Therefore, we have a steady-state solution to work with as long as we run our simulation in an appropriately short time span.

The simulation time span cannot be too short, because we need it to be large enough in order to be able to record the growth rates of our perturbed modes accurately. For, as we have seen in Sec. 6.4, we are not perturbing the vortex along the true eigenvector, and therefore it

takes some time for the system to settle to the unstable eigenvector. We also need to choose our perturbation amplitude so that in the time span we allot, the perturbation does not become too large, where the system's nonlinear effects become relevant. This is because our MI analysis is only valid for small perturbations due to the fact that we relied on linear approximations in Sec. 3.3. With these issues in mind, we choose the following parameters:

$$t_{\text{max}} = 15, \qquad \epsilon = 0.00001, \tag{7.2}$$

where ϵ is our perturbation amplitude to be used in Eq. (6.8). For this time span, the change in K_{crit} and C_3/C_1 for an unperturbed simulation of a vortex of charge $m = 1$ is depicted in Fig. 7.5 (p. 51). We see that the values of the constants change very slightly as mentioned above. Performing simulations of vortices of different charges yield similar results, and therefore we can treat our GN solutions as true steady-state vortices, and use them confidently in testing the predictions for the growth rates.

Now with our selected time span, we run our perturbed simulations. For each charge vortex $m = 1, ..., 5$, we perform a separate simulation for each perturbed azimuthal mode $K = 1, ..., 9$ using the initial condition of Eq. (6.8). Some examples of what vortices perturbed by azimuthal modes look like are shown in Fig. 7.4.

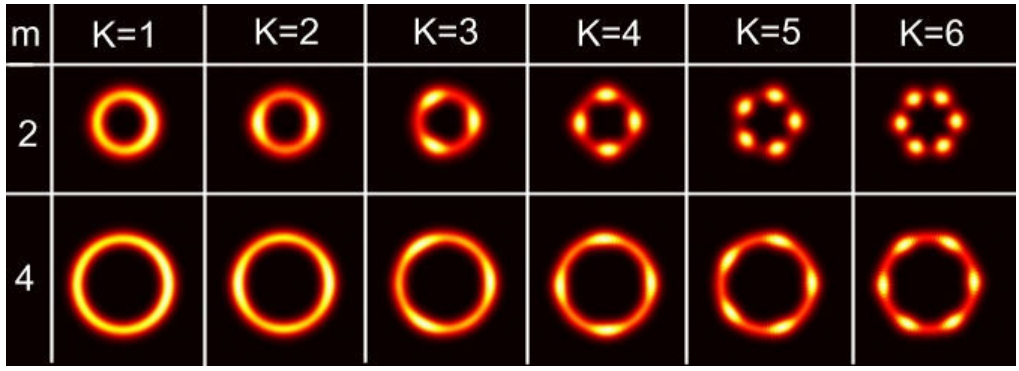

Figure 7.4. Some examples of vortices of charge $m = 2$ and $m = 4$ perturbed by modes $K = 1, ..., 6$ using Eq. (6.8) with $\epsilon = 0.5$. Depicted is a plot of the modulus squared of each perturbed vortex.

During each simulation, we record the average growth rate of the mode being perturbed by the procedure explained in Sec. 6.4. The computed average growth rates for $K = 1, ..., 9$ are then plotted on top of the numerically predicted growth rates for the vortex charge in question taken from Fig. 5.3. The values of both the recorded and predicted growth rates are given in a table below each plot, along with the percent error between the two values.

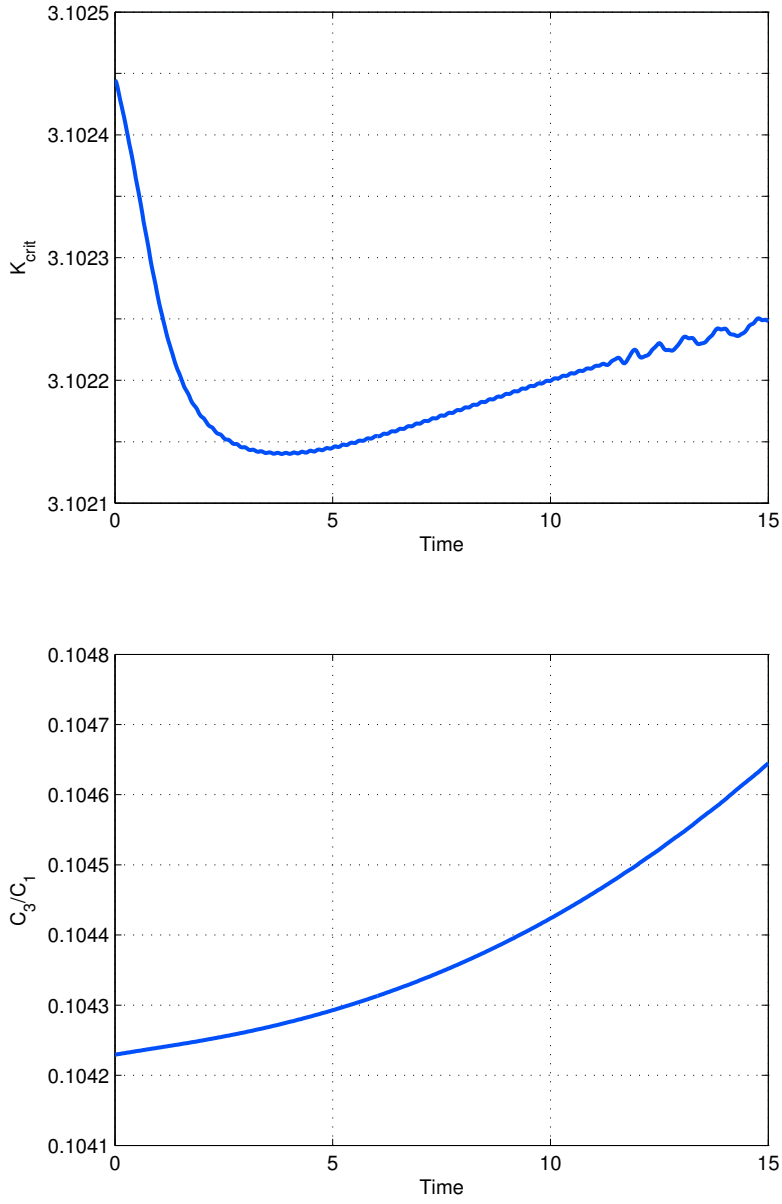

Figure 7.5. Evolution for the values of the predicted critical mode, K_{crit} (top), and prefactor of the predicted growth rates, C_3/C_1 (bottom), over an unperturbed simulation of an $m = 1$ vortex. The simulation is performed using the parameters of Eqs. (7.1) and (7.2). The values for the constants change only slightly, ensuring that the GN solution can be considered steady-state.

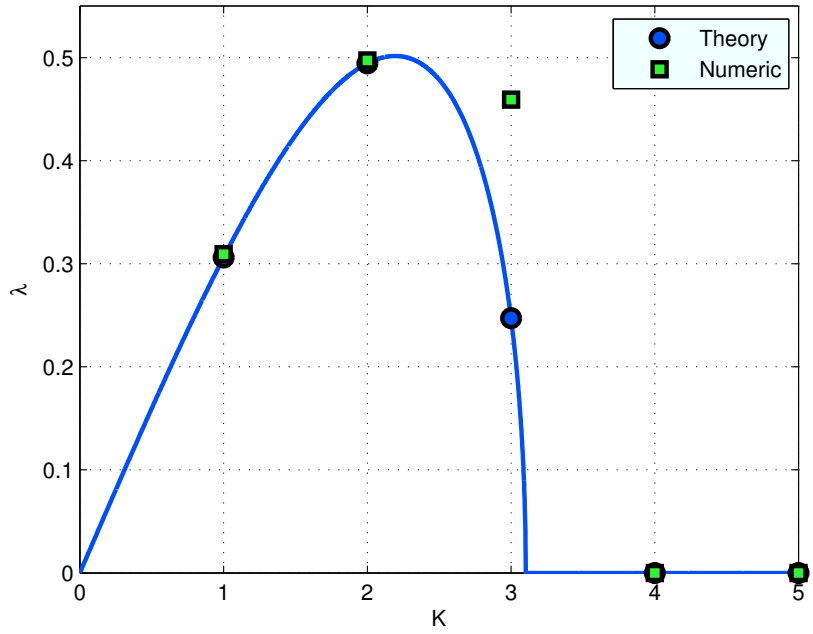

Figure 7.6. Average growth rates from full two-dimensional simulation of vortices of charge $m = 1$ in the NLS perturbed with modes $K = 1, ..., 5$ compared to numerical predictions from the GN profile. The predicted growth rates are shown in blue circles, while the green squares represent the computed growth rates from the full simulation. All numerical parameters are as given in Eqs. (7.1) and (7.2) with $\Omega = 0.25$.

Table 7.1. Numerical Growth Rate Results from Full Simulations and Predictions using GN Profiles for $m = 1$ and $K = 1, ..., 9$ with Percent Error, with all Parameters as Described in Fig. 7.6.

$m = 1$ K :	1	2	3	4	5	6	7	8	9
Result	0.309	0.497	0.459	0	0	0	0	0	0
Predicted	0.306	0.494	0.247	0	0	0	0	0	0
% Error	1.01	0.57	46.16	0	0	0	0	0	0

For a vortex of charge $m = 1$, we get the results depicted in Fig. 7.6 and Table 7.1. We see extremely close agreement between the recorded and predicted growth rates for modes $K = 1$ and $K = 2$, and modes after the critical mode are stable as expected. The prediction

for the growth rate of mode $K = 3$ seems to be almost 50% off, however as we discussed in Sec. 7.1, our simulations for modes near K_{crit} with our azimuthal resolution of $J = 80$ are expected to have errors (in the simulation, not the prediction), and in this case, mode $K = 3$ is very close to the predicted value for the critical mode, $K_{\text{crit}} = 3.10$.

Running simulations on a vortex of charge $m = 2$ yields the results in Fig. 7.7 and Table 7.2.

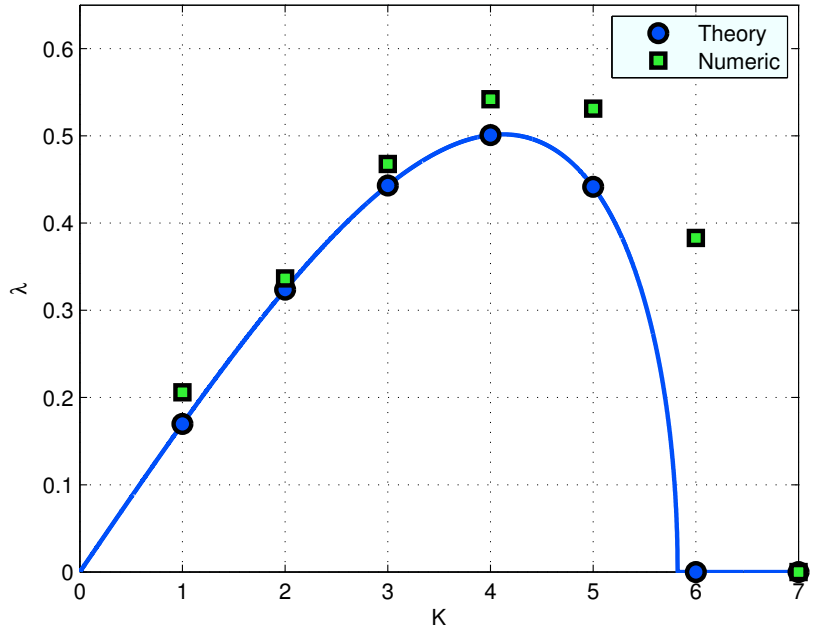

Figure 7.7. Average growth rates from full two-dimensional simulation of vortices of charge $m = 2$ perturbed with modes $K = 1, ..., 5$ compared to numerical predictions. Description of plot and parameters used are the same as in Fig. 7.6.

Table 7.2. Numerical Growth Rate Results from Full Simulations and Predictions using GN Profiles for $m = 2$ and $K = 1, ..., 9$ with Percent Error, with all Parameters as Described in Fig. 7.6.

$m = 2$ | K :	1	2	3	4	5	6	7	8	9
Result	0.206	0.337	0.468	0.542	0.531	0.383	0	0	0
Predicted	0.170	0.324	0.443	0.501	0.442	0	0	0	0
% Error	17.57	3.81	5.27	7.56	16.86	100	0	0	0

We once again see good agreement between the predictions and recorded growth rates, but this time the error is somewhat higher. This error increases as K becomes close to the critical mode as is expected. The critical mode in this case is not predicted correctly, since $K = 6$ should be stable according to the predictions, while in the simulations we record a steady growth rate. This error cannot be accounted for by the resolution issues discussed for the $m = 1$ simulations. It is evident that for all the one-dimensional simulations of the azimuthal equation Eq. (3.3), even with a very coarse resolution, the critical mode was always predicted accurately. Therefore, the error either stems from numerical errors in computing the C-constants of K_{crit}, or because of errors involved in our approximating the vortex with a radial-azimuthal separable solution as discussed in Sec. 2.9.

We have seen in Sec. 5.2 that the Ω which is initially chosen, has errors when recomputed using the dispersion relation. This dispersion relation (Eq. (5.6)) is a function of the C-constants C_1, C_2, C_3, and C_4 and produces an error in Ω of about 1.5% for $m = 2$. The critical mode prediction is made using only C_3 and C_4. Therefore, we cannot directly compare the errors in each, but it is reasonable to suspect that the error in computing the C-constants may be a main factor in the discrepancy between the prediction of K_{crit} and the numerical simulation results.

Running simulations on a vortex of charge $m = 3$ yields the results in Fig. 7.8 and Table 7.3. Here, we see very similar result to those discussed for $m = 2$. The growth rate predictions are within 10% (until K gets close to K_{crit}) and the predicted K_{crit} is one mode off. An important item to notice is that the prediction of the growth rate for mode $K = 5$ is only off by 8%, while for the vortex of charge $m = 2$, where $K = 5$ was close to K_{crit}, the error was $\approx 17\%$. This shows that the resolution sensitivity discussed above and in Sec. 7.1 really is connected with modes near K_{crit}, and not just because we have less azimuthal points for higher modes in general.

Running simulations on a vortex of charge $m = 4$ yields the results in Fig. 7.9 and Table 7.4. For the simulations performed here, and for those for $m = 5$, we do not test our prediction of the critical mode because our azimuthal resolution is not sufficient to reliably simulate modes higher than $K = 9$. With respect to the growth rate predictions, we see that the $m = 4$ case here is very similar to the $m = 3$ case above. The growth rates are generally predicted within $\approx 10\%$ of those recorded from the simulation, and start to increase in error as K approaches K_{crit} (here predicted to be $K_{\text{crit}} = 11.39$).

Running simulations on a vortex of charge $m = 5$ yields the results in Fig. 7.10 and Table 7.5. The results here are once again similar to those for previous vortex charges. One interesting note is that the relative error in predicting the growth rate for $K = 1$ is $\approx 100\%$! However, the absolute error is only around 0.04 which compared to other growth rates is

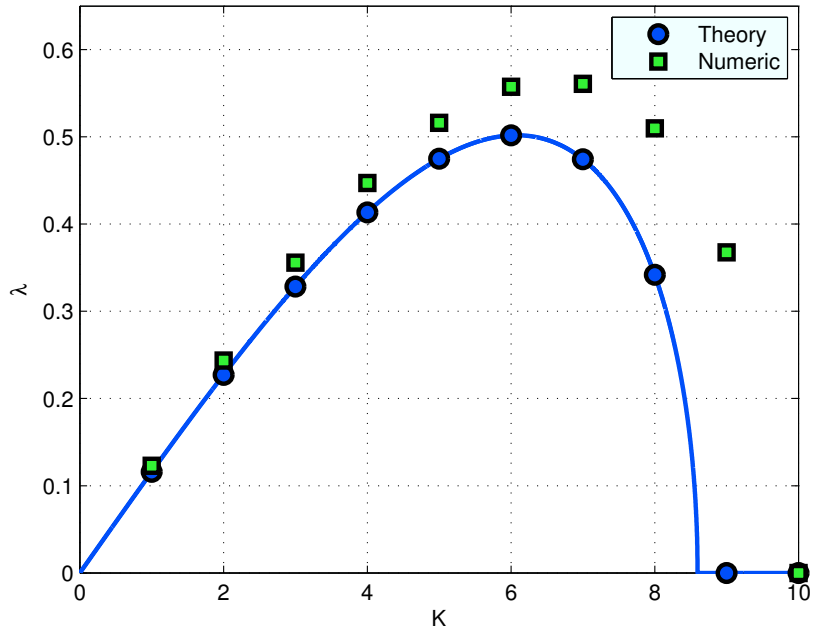

Figure 7.8. Average growth rates from full two-dimensional simulation of vortices of charge $m = 3$ perturbed with modes $K = 1, ..., 5$ compared to numerical predictions. Description of plot and parameters used are the same as in Fig. 7.6.

Table 7.3. Numerical Growth Rate Results from Full Simulations and Predictions using GN Profiles for $m = 3$ and $K = 1, ..., 9$ with Percent Error, with all Parameters as Described in Fig. 7.6.

$m = 3$ | K :	1	2	3	4	5	6	7	8	9
Result	0.123	0.244	0.356	0.447	0.516	0.557	0.561	0.510	0.368
Predicted	0.116	0.227	0.328	0.413	0.475	0.502	0.474	0.342	0
% Error	5.67	6.77	7.73	7.56	8.00	9.99	15.43	32.96	100

small. Also, for this case and especially for charges greater than $m = 5$, the growth rate for $K = 1$ is so small that it is very hard to capture accurately from the simulations.

Overall, we see that our numerical simulations yield growth rates that are close to those predicted, but typically slightly higher, with an error on the order of 10% for modes far from K_{crit}. For modes close to K_{crit}, we observe higher error. Also, for $m = 2$ and $m = 3$, the predicted K_{crit} is one mode off. We have discussed possible reasons for these discrepancies,

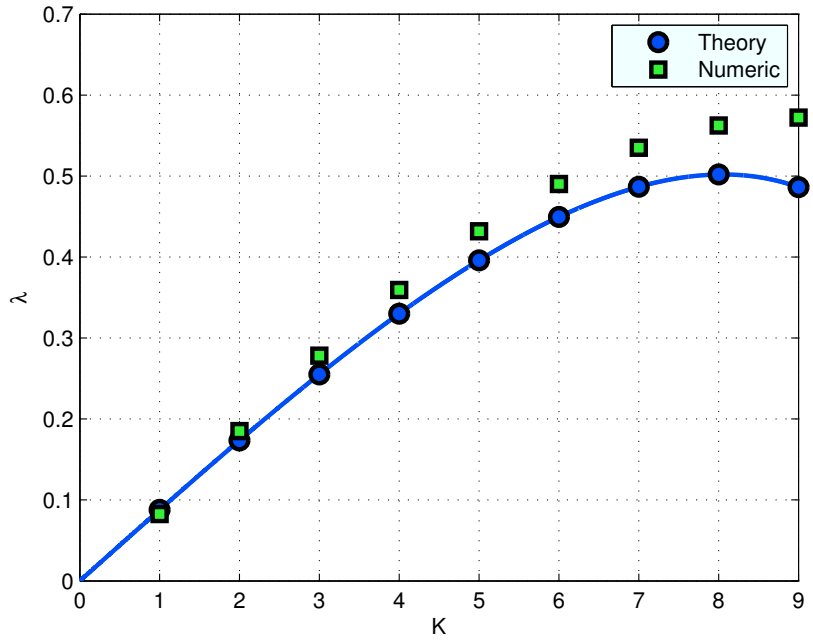

Figure 7.9. Average growth rates from full two-dimensional simulation of vortices of charge $m = 4$ perturbed with modes $K = 1, ..., 5$ compared to numerical predictions. Description of plot and parameters used are the same as in Fig. 7.6.

Table 7.4. Numerical Growth Rate Results from Full Simulations and Predictions using GN Profiles for $m = 4$ and $K = 1, ..., 9$ with Percent Error, with all Parameters as Described in Fig. 7.6.

$m = 4$ K :	1	2	3	4	5	6	7	8	9
Result	0.083	0.185	0.278	0.359	0.432	0.490	0.535	0.562	0.572
Predicted	0.088	0.174	0.255	0.330	0.396	0.449	0.487	0.502	0.486
% Error	6.33	6.20	8.36	8.16	8.30	8.32	9.02	10.75	15.04

some of which (like the resolution issues near K_{crit}) can be minimized (i.e. simulate with very high resolution).

Before we conclude, we briefly show explicitly one of the many possible extensions to the theory, that of the nonlocal case.

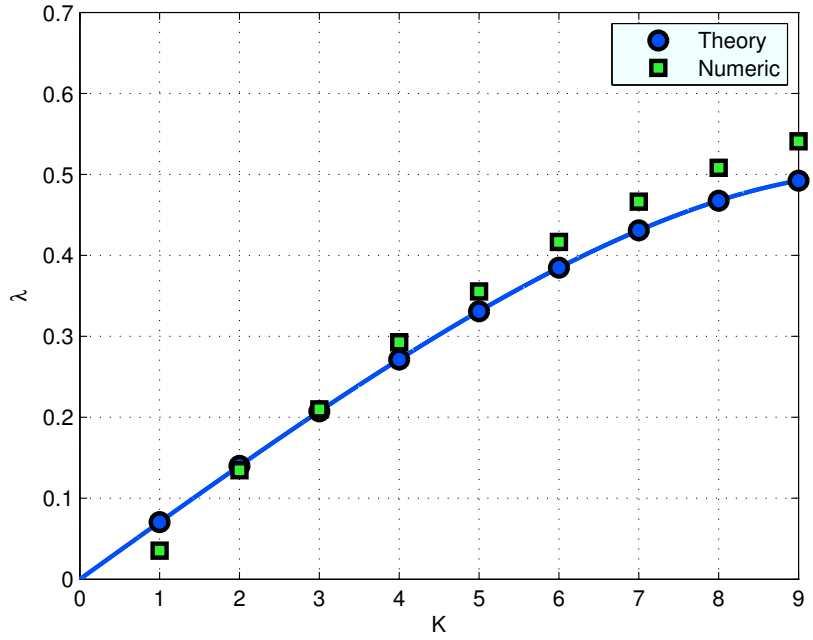

Figure 7.10. Average growth rates from full two-dimensional simulation of vortices of charge $m = 5$ perturbed with modes $K = 1, ..., 5$ compared to numerical predictions. Description of plot and parameters used are the same as in Fig. 7.6.

Table 7.5. Numerical Growth Rate Results from Full Simulations and Predictions using GN Profiles for $m = 5$ and $K = 1, ..., 9$ with Percent Error, with all Parameters as Described in Fig. 7.6.

$m = 5$ | K :	1	2	3	4	5	6	7	8	9
Result	0.035	0.135	0.210	0.293	0.355	0.417	0.466	0.508	0.541
Predicted	0.071	0.140	0.207	0.271	0.331	0.385	0.431	0.467	0.492
% Error	100.3	4.02	1.10	7.23	6.88	7.67	7.63	8.01	8.98

CHAPTER 8

THEORETICAL EXTENSION: THE NONLOCAL CASE

Here we describe one of the possible extensions to the theory, that of incorporating nonlocal interactions. Such interactions correspond to various physical systems, such as dipole-dipole interactions in a BEC of degenerate dipolar atoms [9], and nonlinear crystals whose nonlinear refractive index change due to the intensity of the light present, is determined by a transport process such as heat conduction [20].

8.1 NONLOCAL MODEL

For nonlocal interactions, the NLS can be altered to have a nonlocal nonlinearity as shown in [20]:

$$i\Psi_t + \nabla^2\Psi + sN\left(|\Psi|^2\right)\Psi = 0, \tag{8.1}$$

where the nonlocal nonlinearity, N is:

$$N\left(|\Psi(r,\theta,t)|^2\right) = \int_0^{2\pi}\int_0^{\infty} V((r'-r),(\theta'-\theta))\,|\Psi(r',\theta',t)|^2\,r'\,dr'\,d\theta',$$

and where V, the nonlocal response function, is taken to be a Gaussian (which appears in relation to the nonlinear crystal heat diffusion nonlocality [20]):

$$V(r'-r,\theta'-\theta) = \frac{1}{\pi\sigma^2}\exp\left(-[((r'-r)\cos(\theta'-\theta))^2 + ((r'-r)\cos(\theta'-\theta))^2]\frac{1}{\sigma^2}\right).$$

Formulating the Lagrangian density of Eq. (8.1) yields:

$$\mathcal{L} = \frac{i}{2}\left(\Psi\Psi_t^* - \Psi^*\Psi_t\right) + |\Psi_r|^2 + \left|\frac{1}{r}\Psi_\theta\right|^2 - \frac{s}{2}|\Psi|^2 N(|\Psi|^2)\ ,$$

which, by using the same method as in Chap. 2, we arrive at the following azimuthal equation of motion:

$$i\,C_1 A_t = C_2 A - C_3 A_{\theta\theta} - s\,C(\theta,t)A, \tag{8.2}$$

where C is defined as:

$$C(\theta,t) = \int_0^{2\pi}\int_0^{\infty}\int_0^{\infty} V((r'-r),(\theta'-\theta))\,|f(r)|^2|f(r')|^2|A(\theta',t)|^2 rr'\,dr\,dr'\,d\theta'.$$

8.2 STABILITY ANALYSIS

We use the same stability analysis technique as in Chap. 3, with a slight alteration. We notice that if we define:

$$R(\theta' - \theta) = \int_0^\infty \int_0^\infty V((r' - r), (\theta' - \theta)) \, |f(r)|^2 |f(r')|^2 \, rr' \, dr \, dr',$$

then C is now a convolution term as follows:

$$C(\theta, t) = \int_0^{2\pi} R(\theta' - \theta) |A(\theta', t)|^2 \, d\theta' = R * |A|^2.$$

Inserting this into Eq. (8.2), and making the same simplifications of Eqs. (3.1) and (3.2), yields:

$$iA_t = -A_{\theta\theta} - \frac{s}{C_3} A(R * |A|^2).$$

Now, we perform a stability analysis identical to that of Sec. 3.2, but along with the transforms of $\hat{u}$ and $\hat{v}$, we also add:

$$\hat{R}(K) = \int_0^{2\pi} R(\theta) e^{iK\theta},$$

in which case the convolution term becomes a product ($A\hat{R}$), and we get:

$$\lambda_{1/2} = \pm \frac{C_3}{C_1} \sqrt{K^2 \left(2s \frac{\hat{R}(K)}{C_3} - K^2 \right)},$$

and

$$K_{\text{crit}} = \pm \sqrt{2s \frac{\hat{R}(K)}{C_3}}.$$

We see that depending on the nonlocal response function, K_{crit} can be damped, and if $\hat{R}(K) < \left| \frac{C_3}{2s} \right|$ then $K_{\text{crit}} < 1$ and all modes become stable. Therefore, we see that one could have a vortex in the focusing NLS with a nonlocal nonlinearity which would be modulationally stable. This could have many practical applications, such as data storage and communications using light vortices in a Kerr optical media [7].

CHAPTER 9

CONCLUSION

In this thesis, we have formulated an expandable methodology for studying MI of vortices in the two-dimensional NLS. The method relies on approximating a vortex solution as being separable into its radial and azimuthal parts, and using the Lagrangian functional of the NLS to obtain a quasi-one-dimensional equation of motion for the azimuthal direction. A stability analysis on modular perturbations of the equation, leads to predictions of growth rates for each perturbed mode, and of the critical mode. After obtaining a steady-state vortex solution, we ran numerical simulations of the NLS, perturbing individual modes to test the predictions. We now summarize our results and briefly discuss examples of possible extensions to the NLS which can be studied using our method.

9.1 SUMMARY OF RESULTS

The results from Chap. 7 show that the methodology for MI analysis presented here is valid. Although the growth rates are not predicted perfectly, the predictions do come very close, and usually within 8% of the predicted rates. From the sources of errors discussed in Sec. 7.2, we see that higher resolution simulations should be able to capture the growth rates for modes close to K_{crit} more accurately with respect to the predictions. The prediction of K_{crit}, which is usually the desired information in any application, is very accurate, only being off by at most one mode number.

One key result that should not be overlooked is that of the usefulness of the variational ansatz profile VA2 of Eq. (4.25). As we have seen, this profile seems to converge to the numerically exact solution as $|m| > \infty$. However, as we have noted, our vortex solutions are not separable into radial and azimuthal parts, leading to possible discrepancies in our predictions. We see however, that the two-dimensional vortex solutions become more separable as $|m| > \infty$, thus improving our predictions. For very large $|m|$, the numerical optimization used to find the vortex profile, using a high enough resolution to avoid the errors mentioned in Sec. 5.2, can become very computationally expensive. However, since VA2 converges to the true solution, its analytic stability predictions of Eq. (5.5) can be used without the need to run numerical computations at all. Also, even for low charges, VA2 very accurately describes the radius and maximum intensity of the vortex. This information can be very helpful in designing experiments.

9.2 Further Extensions

The methodology used here to study MI of vortices in the NLS can be extended to other NLS-type systems. One example of this, that of a nonlocal nonlinearity, was shown in Chap. 8. Another extension of interest would be to add an external potential term to the NLS, making the analysis directly relevant to BECs. Such a potential (if radially symmetric) would simply be integrated in the radial direction, and show up as another constant term in Eq. (2.10). Other possible extensions include adding a quintic nonlinearity, relevant to BEC collapse [2], and a saturation nonlinearity, relevant to nonlinear crystals [5]. In general, our MI analysis can include any extension to the NLS, as long as it has a Lagrangian representation. This expandability of the method adds greatly to its usefulness and importance.

BIBLIOGRAPHY

[1] P. G. Kevrekidis, D. J. Frantzeskakis and R. Carretero-González. *Emergent Nonlinear Phenomena in Bose-Einstein Condensates: Theory and Experiment*. Springer, New York, New York, 1 edition, 2007.

[2] M. Ueda and H. Saito. A consistent picture of a collapsing Bose-Einstein condensate. *Journal of the Physical Society of Japan*, **72** (2003) Supplement C, 127–133.

[3] R. Carretero-González, D.J. Frantzeskakis and P.G. Kevrekidis. Nonlinear waves in Bose-Einstein condensates: Physical relevance and mathematical techniques. To appear in Nonlinearity, 2008.

[4] D. E. Pelinovsky, Y. A. Stepanyants and Y. S. Kivshar. Self-focusing of plane dark solitons in nonlinear defocusing media. *Physical Review E*, **51** (1995) 5016 – 5026.

[5] Y. S. Kivshar and B. Luther-Davies. Dark optical solitons: Physics and applications. *Physics Reports 298*, **298** (1998) 81 – 197.

[6] K. W. Madison, F. C., W. Wohileben and J. Dalibard. Vortex formation in a stirred Bose-Einstein condensate. *Physical Review Letters*, **84** (2000) 806–809.

[7] Y. S. Kivshar and E. A. Ostrovskaya. Optical vortices: Folding and twisting waves of light. *Optics and Photonics News*, **12** (2001) 24–28.

[8] Wikipedia. Opticalvortices: http://en.wikipedia.org/wiki/image:opticalvortices.jpg, 2004.

[9] V. M. Lashkin. Two-dimensional nonlocal vortices, multipole solitions and rotating multisolitons in dipolar Bose-Einstein condensates. *Physical Review A*, **75** (2007) 043607.

[10] R. M. Caplan, R. Carretero-González, P.G. Kevrekidis and Q. E. Hoq. Modulational instability of vortices in a two-dimensional nonlocal medium. In progress, 2008.

[11] L. Debnath. *Nonlinear Partial Differential Equations for Scientists and Engineers*. Birkhauser Boston, New York, New York, 2 edition, 2005.

[12] B. Malomed. Variational methods in nonlinear fiber-optics and related fields. *Progress in Optics*, **43** (2002) 71–193.

[13] W.Krolikowski, O. Bang, J. J. Rasmussen and J. Wyller. Modulational instability in nonlocal nonlinear kerr media. *Physical Review E*, **64** (2001) 016612.

[14] D. Briedis, D.E. Petersen, D. Edmundson, W. Krolikowski and O. Bang. Ring vortex solitons in nonlocal nonlinear media. *Optics Express*, **13** (2005) 435–443.

[15] J. Nocedal and S. J. Wright. *Numerical Optimization*. Springer, New York, New York, 2 edition, 2006.

[16] L. D. Carr and C. W. Clark. Vortices in attractive Bose-Einstein condensates in two dimensions. *Physical Review Letters*, **97** (2006) 010403.

[17] V. V. Afanasjev. Rotating ring-shaped bright solitons. *Physical Review E*, **52** (1995) 3153–3158.

[18] G. H. Golub and J. M. Ortega. *Scientific Computing and Differential Equations An Introduction to Numerical Methods*. Academic Press, San Diego, California, 2 edition, 1992.

[19] J. C. Strikwerda. *Finite Difference Schemes and Partial Differential Equations*. Society for Industrial and applied Mathematics, Philadelphia, PA, 2 edition, 2004.

[20] J. Wyller, W. Krolikowski, O. Bang and J. J. Rasmussen. Generic features of modulational instability in nonlocal Kerr media. *Physical Review E*, **66** (2002) 066615.

ABSTRACT OF THE THESIS

Azimuthal Modulational Instability
of Vortex Solutions to the
Two Dimensional Nonlinear Schrödinger Equation
by
Ronald Meyer Caplan
Master of Science in Computational Science
San Diego State University, 2008

We study the azimuthal modulational instability (MI) of vortices with different topological charges, in the focusing two-dimensional nonlinear Schrödinger (NLS) equation. This setting has direct application in the realm of Bose-Einstein condensates and light propagation in nonlinear crystals.

The method of studying the stability relies on freezing the radial direction in the Lagrangian functional of the NLS in order to form a quasi-one-dimensional azimuthal equation of motion, and then applying a stability analysis in Fourier space of the azimuthal modes. We formulate predictions of growth rates of individual modes and find that vortices are unstable below a critical azimuthal wave number.

Steady state vortex solutions are found by first using a variational approach to obtain an asymptotic analytical ansatz, and then using it as an initial condition to a nonlinear equation numerical optimization routine. The stability analysis predictions are corroborated by direct numerical simulations of the NLS performed on a polar coordinate finite-difference scheme.

We briefly show how to extend the method to encompass nonlocal nonlinearities that tend to stabilize solutions.